


Article

Photocatalytic Bactericidal Performance of LaFeO₃ under Solar Light in the Presence of Natural Organic Matter: Spectroscopic and Mechanistic Evaluation

Nazmiye Cemre Birben ^{1,*}, Ezgi Lale ¹, Renato Pelosato ² , Nazli Turkten ³, Isabella Natali Sora ² and Miray Bekbolet ¹ 

¹ Institute of Environmental Sciences, Bogazici University, Istanbul 34342, Turkey; ezgilale91@gmail.com (E.L.); bekbolet@boun.edu.tr (M.B.)

² INSTM and Department of Engineering and Applied Sciences, University of Bergamo, 24044 Dalmine, Italy; renato.pelosato@unibg.it (R.P.); isabella.natali-sora@unibg.it (I.N.S.)

³ Department of Chemistry, Faculty of Arts and Sciences, Kirsehir Ahi Evran University, Kirsehir 40100, Turkey; nazli.turkten@ahievran.edu.tr

* Correspondence: cemre.birben@boun.edu.tr

Abstract: Solar photocatalytic inactivation (SPCI) of *E. coli* as the indicator microorganism using LaFeO₃ (LF) has already been investigated under various experimental conditions, excluding any role of natural organic matter (NOM). However, comprehensive information about the behavior of *E. coli* and its inactivation mechanism in the presence of NOM, as well as the behavior of NOM components via solar photocatalysis using LF as a photocatalyst, has prime importance in understanding real natural water environments. Therefore, in this study, further assessment was devoted to explore the influence of various NOM representatives on the SPCI of *E. coli* by using LF as a novel non-TiO₂ photocatalyst. The influence of NOM as well as its sub-components, such as humic acids (HA) and fulvic acids (FA), was also investigated to understand different NOM-related constituents of real natural water conditions. In addition to spectroscopic and mechanistic investigations of cell-derived organics, excitation emission matrix (EEM) fluorescence spectra with parallel factor multiway analysis (PARAFAC) modeling revealed further information about the occurrence and/or disappearance of NOM-related and bacteria-related fluorophores upon LF SPCI. Both the kinetics as well as the mechanism of the LF SPCI of *E. coli* in the presence of NOM compounds displayed substrate-specific variations under all conditions.

Keywords: *E. coli*; lanthanum orthoferrite; natural organic matter; PARAFAC modeling; perovskite; photocatalytic inactivation



Citation: Birben, N.C.; Lale, E.; Pelosato, R.; Turkten, N.; Natali Sora, I.; Bekbolet, M. Photocatalytic Bactericidal Performance of LaFeO₃ under Solar Light in the Presence of Natural Organic Matter: Spectroscopic and Mechanistic Evaluation. *Water* **2021**, *13*, 2785. <https://doi.org/10.3390/w13192785>

Academic Editor: Sergi Garcia-Segura

Received: 31 July 2021

Accepted: 3 October 2021

Published: 8 October 2021

Publisher's Note: MDPI stays neutral with regard to jurisdictional claims in published maps and institutional affiliations.



Copyright: © 2021 by the authors. Licensee MDPI, Basel, Switzerland. This article is an open access article distributed under the terms and conditions of the Creative Commons Attribution (CC BY) license (<https://creativecommons.org/licenses/by/4.0/>).

1. Introduction

Natural organic matter (NOM) is known to be originated from the residues of plants and microbial components or could be derived from water cycles and/or various decomposition pathways [1]. NOM in natural waters comprises a variety of amphiphilic components, of which the major fraction (>50% of total organic carbon) is related to hydrophobic acids, including humic acids (HA), fulvic acids (FA), and humin. Differentiation of HA and FA could be ascribed to variations in molecular weight, the number of functional groups (carboxyl and phenolic OH), and the extent of polymerization. In general, FA have lower molecular weights than HA, which play a crucial role in the interactions between NOM components and other organic and inorganic constituents of aquatic environments. Being regarded as the major organic fraction of natural water sources, NOM components would have a critical function in the physicochemical as well as photochemical reaction pathways. Moreover, the performance of unit processes, the application of chemicals in water treatment processes, and the biological stability of water are all dependent on the

quantity and quality of NOM in water sources; therefore, it plays a crucial role in the design, selection, and operation of water treatment processes [2].

Photochemical advanced oxidation processes (AOPs) are attractive alternatives to non-destructive physical water treatment processes due to their ability to mineralize organic water contaminants. In addition, the disinfection capability of AOPs also has prime importance in preventing the spread of infectious waterborne diseases. Among all different AOPs, photocatalytic disinfection using a semiconductor photocatalyst has gained special interest for decades and has been reported in the literature [3–5]. Further assessment of novel photocatalytic materials, such as doped TiO₂ specimens and other metal oxides, nanocomposites, non-TiO₂ materials, and their modified versions, such as perovskites and perovskite-like materials, has attracted wide attention. Metal oxides are the most stable materials in terms of light absorbing in water. A potential solar photocatalyst may be a perovskite-type oxide, with the general formula ABO₃, considering that the perovskite structural family exhibits nearly every type of electronic behavior shown by oxides. Among perovskites, lanthanum orthoferrite (LaFeO₃) is reported to be a promising solar photocatalyst. Detailed information related to the application of perovskites and perovskite-like materials to solar photocatalytic antimicrobial activities was presented previously by Birben et al. [6]. Moreover, in this previous study, solar photocatalytic inactivation kinetics of *E. coli* using LaFeO₃ as the photocatalyst was investigated profoundly by the consideration of various aqueous medium matrices. Consisting of 0.85% NaCl, saline solution (SS) was used to maintain a survival medium to understand *E. coli* inactivation in order to exclude any organic and other inorganic constituents. A water matrix (WM), which was defined as a synthetic solution matrix comprising major cation and anion contents of natural waters, was prepared and used in the experiments. For the representation of the base reaction medium free of any organic and inorganic constituents of natural water conditions, ultrapure water (MQ) was selected as another matrix, whereas distilled/deionized water (DW) was chosen to eliminate the effect of all ionic constituents. In addition to the kinetic evaluation, a mechanistic approach was also followed for the detection of bacterial-cell-derived organics and inorganics by addressing the most appropriate analytical techniques (the Lowry method for protein detection, organic carbon content analysis for carbohydrates, standard methods for K⁺ detection) to understand the destructive impact of solar photocatalytic inactivation process. In contrast, the major organic fraction of natural waters, namely NOM, has not been taken into consideration for its impact on the solar photocatalytic inactivation (SPCI) of pathogenic bacteria. In accordance with the application as a perovskite specimen, solar LF photocatalysis of HA as NOM representatives was also comprehensively studied and elucidated by Turkten et al. [7].

Referring to previous literature findings about the antimicrobial activity as well as different photocatalyst properties of LF, this study aimed to assess the use of LF as a novel non-TiO₂ nanomaterial for the SPCI of *E. coli* as the indicator organism present in drinking water sources. Suwannee River natural organic matter (SRNOM), Suwannee River humic acids (SRHA), and Suwannee River fulvic acids (SRFA) were selected as representatives of NOM compounds for the assessment of the influence of the organic matrix on the SPCI of *E. coli* in the presence of LF as a photocatalyst. In addition to traditional analytical tools, and besides UV–VIS, fluorescence, and FTIR spectroscopic techniques, an advanced fluorescence approach in combination with parallel-factor multi-way analysis as PARAFAC modeling was used to elucidate alterations in NOM components as well as in bacteria-derived constituents under oxidative conditions.

2. Materials and Methods

2.1. Materials

2.1.1. Photocatalyst Specimen: LaFeO₃

The LaFeO₃ photocatalyst was prepared via combustion synthesis. Nitrate salts of lanthanum and iron were mixed in an aqueous solution with citric acid as a complexing agent. Ammonia was then added to the solution until neutral pH was reached. After

evaporation of the solution, a green-brownish gel was obtained, which upon heating rapidly burned to produce fluffy ashes. The ashes were then calcined at 600 °C to get rid of the residual organic matter. More detailed information about the preparation and characterization of LF has been previously presented elsewhere [6–8].

2.1.2. NOM Representatives: SRNOM, SRHA, and SRFA

SRNOM, SRHA, and SRFA as representatives of NOM compounds were purchased from the International Humic Substances Society (IHSS). All NOM representatives were prepared by using distilled/deionized water and continuously stirred overnight to ensure complete dissolution. Stock solutions (200 mg/L) of SRNOM, SRHA, and SRFA were kept in amber glass bottles, and appropriate dilutions were made to prepare working solutions. Considering recent studies related to the organic carbon content of natural waters, the organic carbon content of working solutions of NOM compounds was arranged to be in the range of 3–5 mgOrgC/L. Spectroscopic characterization of NOM representatives was presented in detail in SI (Figures S1 and S2 and Table S1).

2.1.3. Indicator Organism: *E. coli*

An *E. coli* K12 (ATCC 23716) suspension was prepared in Luria–Bertani broth displaying an initial count of colony forming units as 10^5 – 10^6 CFU/mL [6].

2.2. Methodology

All experimental setup as well as a methodology related to solar photocatalytic degradation and inactivation processes were followed according to the previously presented protocol [6,7]. SPCI experiments were carried out using an Atlas Suntest CPS+ solar simulator (Atlas, IL, USA) equipped with an air-cooled xenon lamp with an emission wavelength range of $\lambda = 300$ – 800 nm and light intensity $I_0 = 250$ W/m². Photocatalyst loading was kept constant as 0.50 mg/mL for all conditions, and all runs were conducted using a 100 mL sample volume. Solar photocatalytic degradation experiments of sole SRNOM, SRHA, and SRFA solutions using LF were also performed in order to obtain background information about SPCI. Following SPCI, along with bacterial enumeration and hydrodynamic particle size distribution analyses, LF was removed from the aqueous medium by filtration before proceeding to spectroscopic analyses, as well as for the detection of cellular components. Detailed information about the analytical methodology is presented in the following sections.

2.2.1. *E. coli* Enumeration

E. coli enumeration was performed using the drop-plate method. Depending on the expected *E. coli* counts, appropriate serial dilutions (10^{-3} to 10^{-1} and even direct sampling) were prepared, and each diluted sample was inoculated in triplicate. Inoculated plates were incubated at 44 °C overnight, following which bacteria enumeration in CFU/mL was performed by visual counting (max. 200 colonies/plate, standard error <10%). Following sampling for bacteria enumeration and hydrodynamic particle size distribution determination, the total remaining volume of the samples was filtered through a 0.45 µm membrane filter prior to further analyses [6].

2.2.2. Spectroscopic Characterization

UV–VIS and fluorescence spectroscopic characterization of organic matter were performed under all conditions. The analytical methodology referring to UV–VIS and fluorescence spectroscopy as well as all of the derived spectroscopic parameters were followed according to the procedures previously reported [6]. An advanced fluorescence technique named excitation emission matrix (EEM) was also used for the qualitative evaluation of individual fluorophores prior to and following SPCI. Decomposition and further evaluation of clustered fluorophores were assessed by EEM fluorescence spectra in combination with

PARAFAC modeling. Detailed information about the methodology related to EEM and PARAFAC modeling is given below.

EEM contour plots were constructed based on the fluorescence data recorded at excitation wavelengths of 200–500 nm with 10 nm steps and emission wavelengths of 200–600 nm with 0.5 nm steps. EEM contour plots were plotted as the fluorescence intensity with respect to emission and excitation wavelengths by using Matlab 2013a. Fluorophoric regions were elucidated according to regional speciation defined in the literature. In general, NOM exhibits fluorescence in an excitation wavelength range of $\lambda_{\text{exc}} = 200$ to 500 nm and an emission wavelength range of $\lambda_{\text{emis}} = 280$ to 600 nm, as observed in EEM fluorescence contour plots. More specifically, regional evaluation of EEM contour plots could be presented as follows: region I, aromatic proteins I ($\lambda_{\text{exc}} = 220$ –250 nm and $\lambda_{\text{emis}} = 280$ –332 nm); region II, aromatic proteins II ($\lambda_{\text{exc}} = 220$ –250 nm and $\lambda_{\text{emis}} = 332$ –380 nm); region III, fulvic-like fluorophores ($\lambda_{\text{exc}} = 220$ –250 nm and $\lambda_{\text{emis}} = 380$ –580 nm); region IV, microbial by-products ($\lambda_{\text{exc}} = 250$ –470 nm and $\lambda_{\text{emis}} = 280$ –380 nm); and region V, humic-like fluorophores ($\lambda_{\text{exc}} = 250$ –470 nm and $\lambda_{\text{emis}} = 380$ –580 nm) [9–11]. PARAFAC modeling was conducted using EEM fluorescence data and the DOMFluor Toolbox in Matlab 2013a according to the recommended procedure [12]. PARAFAC belongs to a family of so-called multi-way methods applicable to data that are arranged in three- or higher-order arrays. Fluorescence EEMs (sample–excitation wavelength–emission wavelength), chromatographic data (GC-MS: sample–elution time– m/z structure), sensory data (sample–attribute–judge), and electroencephalography (space–time–frequency) are some of the examples of three-way arrays that could be analyzed by the PARAFAC model by which three-way data sets decompose the data signal into a set of trilinear terms and a residual array:

$$X = \sum_{f=1}^F a_{if}b_{jf}c_{kf} + e_{ijk} \quad (1)$$

where $i = 1, \dots, I$; $j = 1, \dots, J$; and $k = 1, \dots, K$. According to Equation (1), X_{ijk} is the data point corresponding to the i -th sample at the j -th variable on mode 2 and at the k -th variable on mode 3 and e_{ijk} is the residual representing the variability not accounted for by the model. In the case of a fluorescence excitation–emission matrix, i , j , and k correspond to the sample, emission mode, and excitation mode, respectively. Each f corresponds to a PARAFAC component, and each such component has I a -values (scores), one for each sample. Each component also has J b -values, one for each emission wavelength, as well as K c -values, one for each excitation wavelength. Detailed information about the methodology related to EEM and PARAFAC is given below.

Fluorescence EEM contour plots of all samples upon exposure to solar photocatalytic degradation in the absence (36 samples) and presence (34 samples) of NOM were successfully decomposed by the PARAFAC model for the identification of the number, type, and intensity of individual fluorescent NOM components. A stepwise analytical procedure was followed: (i) importing raw data sets to visualize each EEM contour -plot; (ii) preprocessing the data set, which includes correcting biases and the removal of Rayleigh and Raman peaks to prevent scattering; (iii) identification and removal of outliers from the data set, based on instrument errors, artifacts, and discrepancy with other samples, which was processed via an exploratory analysis using non-negative constraints that constituted the outlier detection and visualization of the residuals; (iv) validation of the model including determination of the number of components, evaluation of model fit, and sensitivity analyses; and (v) validation of the number of components distinguished by the PARAFAC model by split-half analysis, followed by visualizing PARAFAC components and obtaining F_{max} values for each sample.

FTIR spectroscopic analyses were performed on selected samples that were prepared by filtration through 0.45 μm membrane filters. Filter papers were placed on a Petri dish and dried at 25 ± 2 °C, with the lids on. ATR-FTIR spectra were recorded between $\nu 4000$ and 400 cm^{-1} on a Nicolet 6700 spectrophotometer (Thermo Fisher Scientific, Waltham,

MA, USA) equipped with an ATR sampling device containing a diamond crystal. The spectra were scanned at room temperature in transmission mode with a spectral resolution of 4.0 cm^{-1} . Each spectrum corresponded to an average of 32 scans, using blank filter paper as a reference under the same instrumental conditions before each series of measurements. Processing of the exported data was carried out with the optical spectroscopy software SpectraGryph (F. Menges, Spectragryph-optical spectroscopy software, 1 (2020), version 1.2.14, <http://www.ffmpeg2.de/spectragryph/> (accessed on 2 April 2021)).

2.2.3. Detection of Cellular Contents upon Cell Lysis

Release of cellular components upon the SPCI of *E. coli* in the presence of NOM representatives was assessed in terms of protein, K^+ , and dissolved organic carbon (DOC) contents according to the methodology presented previously by Birben et al. [6]. A Shimadzu Vwp TOC analyzer was used for the determination of the DOC content (mg/L) in non-purgeable organic carbon mode. The Lowry method was used to elucidate the total protein content of the sample solutions. The total K^+ content was determined based on the methodology given in standard methods of the 3500-K B flame photometric method. Detailed explanations of the DOC measurement, the Lowry method, and determination of the K^+ content were all presented by Birben et al. previously [6].

2.2.4. Additional Analysis

Hydrodynamic particle size distribution profiles of LF under specified experimental conditions and zeta potential measurements in the presence of NOM analogues prior to and following SPCI were performed by using the 90 Plus Particle Size/Zeta Analyzer (Brookhaven Instruments, Holtsville, NY, USA).

3. Results

3.1. SPCI in the Presence of Various NOM Analogues Using LF

3.1.1. Bacterial Inactivation Profiles

Upon LF SPCI in the presence of NOM analogue compounds, *E. coli* cell counts displayed a decaying profile with irradiation time, as presented in Figure 1 and Table 1. Almost all of the bacteria were inactivated in 30 min following the trend $\text{SRFA} \approx \text{SRHA} > \text{SRNOM}$. Upon a further irradiation period of 40 min, the effect of SRNOM leveled off to both SRHA and SRFA. The SPCI of *E. coli* using LF in the presence of NOM analogue compounds followed pseudo first-order kinetics irrespective of the type of the organic matrix. *E. coli* logarithmic reduction profiles indicated that kinetics could well be expressed by the first-order kinetic model, as previously expressed, determined and explained by Birben et al. [6].

In the presence of NOM analogue compounds, significant enhancement was attained with respect to inactivation kinetics observed in SS ($k = 0.0335\text{ min}^{-1}$, rate = $3.49 \times 10^4\text{ CFU/mL min}$) and WM ($k = 0.150\text{ min}^{-1}$, rate = $1.29 \times 10^5\text{ CFU/mL min}$) [6]. The reason of retardation could be attributed to the presence of common anions in the WM composition that significantly altered HO^\bullet formation as well as consumption mechanisms. Inactivation rate constants expressed that SRFA and SRHA exert almost similar effects on *E. coli* reduction, whereas SRNOM expressed a slightly lower rate constant. With respect to the previous findings attained for the SPCI of *E. coli* under various conditions, excluding the effect of any organic constituents (SS, DW, WM, and MQ), kinetic parameters in SRHA and SRFA expressed similar outcomes under the MQ condition ($k = 0.349\text{ min}^{-1}$, rate = $3.37 \times 10^5\text{ CFU/mL min}$) that represented the ultrapure water medium. Although NOM analogues contained significant amount of organic carbon in comparison to the MQ condition, similar kinetic data of these distinctly different reaction conditions could be attributed to the effect of osmotic pressure created by MQ water that burst *E. coli* cells rather than the SPCI mechanism. Enhancement of the SPCI kinetics of *E. coli* could be ascribed to the photochemical properties of NOM analogues that could act as photosensitizers and therefore produce reactive species. Consequently, NOM-originated reactive species would tend to attack *E. coli* cells, leading to their inactivation. Since surface interactions prior to initiation

of solar photocatalysis could not be assessed quantitatively, binary, and ternary interactions should be evaluated for the understanding of the reaction mechanism.

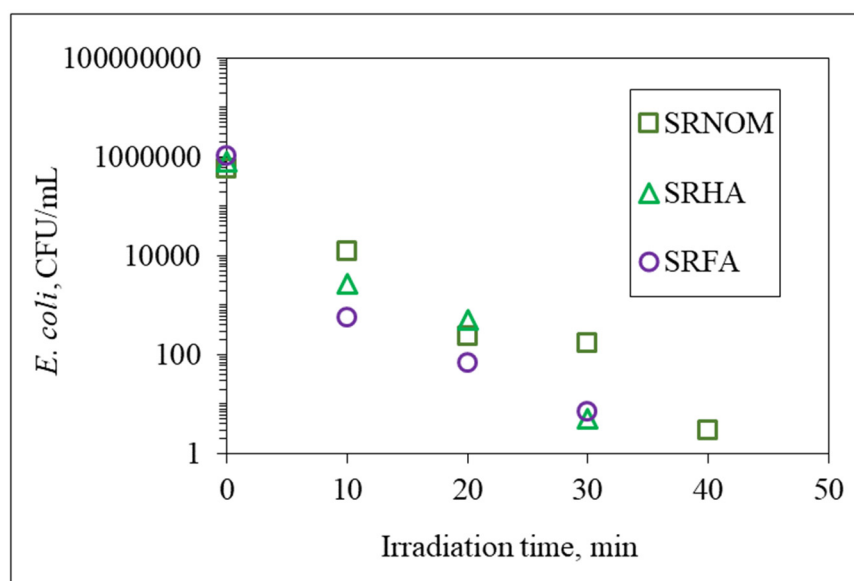


Figure 1. SPCI profile of *E. coli* using LF in the presence of NOM analogue compounds.

Table 1. SPCI of *E. coli* in the presence of NOM analogue compounds: kinetic parameters.

| NOM | k, min^{-1} | $t_{1/2}, \text{min}$ | Rate, CFU/mL min |
|-------|----------------------|-----------------------|--------------------|
| SRNOM | 0.287 | 2.42 | 2.66×10^5 |
| SRHA | 0.376 | 1.84 | 3.61×10^5 |
| SRFA | 0.379 | 1.83 | 3.98×10^5 |

Various competing and contributing factors should be addressed in order to visualize the reaction medium consisting of bacteria (*E. coli* cells), NOM analogue compounds (SRNOM, SRHA, and SRFA), organic sub-fractions (formed by cell destruction), and inorganic surface (LF). Regarding the surface-oriented nature of photocatalysis, the potential role of all possible surface interactions was extensively discussed and reported by Uyguner et al. [4].

Surface charge effects leading to binary and ternary system surface interactions could be described as follows:

Mono System Properties

E. coli as a Gram-negative bacterium has a cell wall composed of an outer membrane containing phospholipids, lipoproteins, lipopolysaccharides (LPS), and proteins, in addition to a peptidoglycan layer. Bacterial cell walls expose numerous carboxyl, phosphate, and phenolic functional groups to the aqueous phase and are negatively charged at pH values above approximately 2–3 due to deprotonation of these functional groups, revealing an isoelectric point of *E. coli* at pH 5.5 [13,14]. Further assessment of surface stability was referred to the zeta potential of *E. coli* in the presence of NOM analogue compounds, which were found to be -18.85 mV, -11.50 mV, and -11.78 mV for SRNOM, SRHA, and SRFA, respectively. Therefore, under all experimental conditions, the *E. coli* suspension exerted a negative charge to further particle–particle electrostatic interactions.

As for NOM compounds, charge development on NOM sub-fractions was also pH dependent with reference to the presence of carboxylic (pH 3–5) and phenolic (pH > 8) groups [15]. The number of carboxyl groups was indicated in decreasing order as SRFA > SRNOM > SRHA and the number of phenolic groups as SRHA > SRNOM > SRFA (Table S2). The LF surface charge dominated at $\text{pH}_{\text{zpc}} = 8.9$, since the solution pH was 6–7,

this value being lower than pH_{zpc} at which the LF surface is mostly positively charged. Therefore, electrostatic attractions could be expected between *E. coli*, organics, and the LF surface. Since *E. coli* is considerably larger in size (*E. coli* length = 1–2 μm and diameter = 0.5–1 μm), both organic sub-fractions and LF would be directed to the cells. Scanning electron microscopy (SEM) images of the aggregate size clusters of LF were reported as 40–70 nm, whereas X-ray diffraction (XRD) measurements revealed a crystallite size of 43 nm [16].

Binary System Interactions

Binary system interactions were mainly discussed as prevailing between different species rather than homo-type binary interactions, i.e., LF–LF (aggregation/agglomeration), *E. coli*–*E. coli* (repulsive forces), and intra- and inter-NOM sub-fractions (polydispersity, conformational changes, re-organization, etc.) [17]. During the dynamic experimental conditions provided by continuous stirring of the reaction medium, the major driving force would be electrostatic attraction. The working pH conditions of all samples in solar photocatalytic treatment were almost neutral (pH = 6–7); therefore, electrostatic interaction was expected to prevail between *E. coli* and LF, leading to attachment of LF onto *E. coli*. Cell appendages (i.e., pili, fimbriae, flagella) could readily overcome the initial bacteria–surface repulsions occurring between charged sites. *E. coli* cells could display cell–surface attachment through weak, long-range electrostatic and van der Waals forces, and hydrophobic cell–substratum interactions in a reversible manner; however, irreversible attachment could also be achieved through stronger forces, such as hydrogen and covalent bonding and hydrophobic interactions, combined with contributions from cellular surface structures (fimbriae, flagella, lipopolysaccharides, etc.) [18].

Furthermore, interactions prevailing between LF and NOM analogue compounds could be visualized through previously reported studies performed by using 100 kDa and 30 kDa molecular size fractions of HA [7]. However, membrane stress exerted by solid particles through direct contact leading to cell damage was not expected due to the spherical shape of LF particles [19,20].

Ternary Interactions Prevailing between *E. coli*, NOM Analogue Compounds, and LF

Excluding homo-interactions and as a result of competing and contributing forces, both humic functional groups of organic sub-fractions and those on bacterial surfaces could display high affinities toward the LF surface [17]. Therefore, the hydrodynamic size of the particulate system expressed variations as measured by the dynamic light scattering technique as presented in Figure 2.

The average hydrodynamic particle size of LF was found to be 1556 nm in sole SS in the absence of *E. coli*, 1051 nm in the presence of SRNOM, 991 nm in the presence of SRHA, and 1109 nm in the presence of SRFA. Upon introduction of *E. coli*, the hydrodynamic particle size of the LF and *E. coli* binary system decreased to 1173 nm, and upon further addition of SRNOM, the hydrodynamic size increased to 2280 nm. The ternary system including LF, *E. coli*, and SRHA revealed a hydrodynamic particle size of 1152 nm, while the LF, *E. coli*, and SRFA system expressed a hydrodynamic particle size of 1231 nm. Introduction of *E. coli* into the LF/NOM system ended up with increased hydrodynamic particle sizes under all conditions in comparison to LF/NOM systems. Although *E. coli* and LF as well as SRNOM and LF binary systems displayed no differences, the ternary system comprising *E. coli*, LF, and SRNOM showed a distinct trend in the particle size distribution profile, which could be attributed to potential aggregate formation of LF particles in the presence of NOM and bacterial cells. Shape-controlled reactivity, spherical SEM images of LF, and surface interactions could only be governed by conformational changes of type-dependent organic matter, leading to diverse orientation. *E. coli* cell surfaces are prone to coating by organic matter via electrostatic interactions [21]. Extracellular polymeric substance (EPS), which are mainly composed of polysaccharides and polypeptides, are synthesized and secreted outside of the cell wall by bacteria. Bacteria can embed themselves in EPS having

an apparently negative electric charge ($\epsilon = -14 \sim -38$ mV) that could lead to sequestration of LF particles [22,23]. NOM analogue compounds could also be adsorbed onto LF particles expressing the corona effect [24]. Furthermore, NOM sub-fractions could form bridges between free LF particles adsorbed onto *E. coli* cells. LF particles could also be encapsulated within the “cage” of the organic matrix.

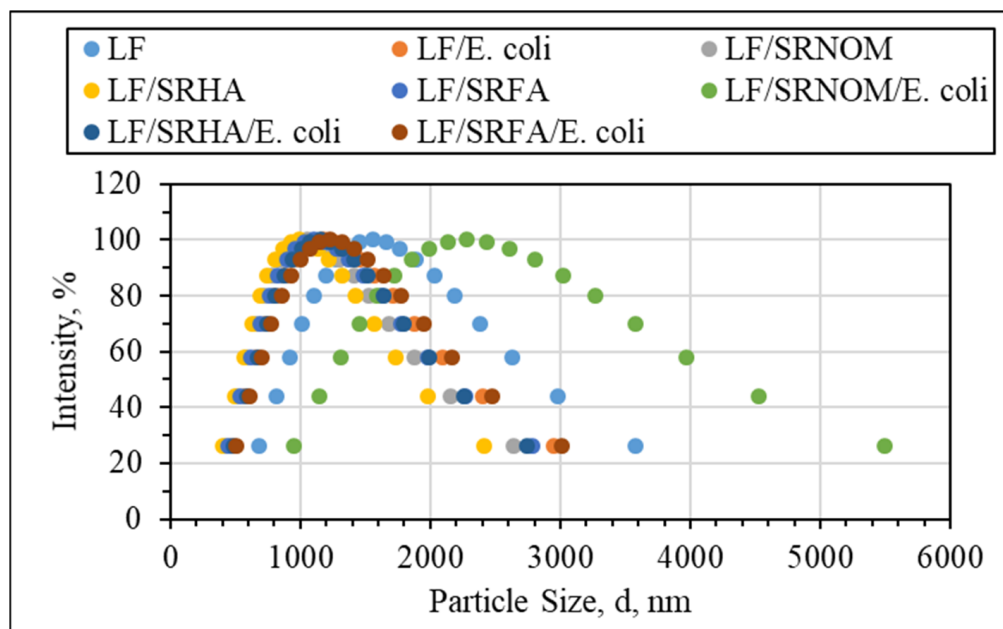


Figure 2. Hydrodynamic particle size distribution profiles of LF for binary and ternary systems.

3.1.2. Spectroscopic Detection of Cellular Constituents Released upon SPCI

3.1.2.1. UV–VIS and Synchronous Scan Fluorescence Spectroscopic Evaluation

UV–VIS absorption spectral features displayed a decaying profile of absorbance with respect to increasing wavelength (Figure 3). SRNOM_i, SRHA_i, and SRFA_i represent sole NOM analogue compounds, the initial represents the organic matrix obtained by successive filtration through 0.45 μm and 0.22 μm membrane filters right after addition of *E. coli* to the solution matrix in the absence of LF, and $t = 0$ represents organic matrix obtained by successive filtration through 0.45 μm and 0.22 μm membrane filters in the presence of NOM and *E. coli* and LF. The extent of the initial adsorption of humic sub-fractions onto LF both in the presence and in the absence of *E. coli* could also be visualized by initial adsorption data of humic UV–VIS parameters. In the absence of *E. coli*, the initial adsorption of SRNOM onto LF revealed a 50–60% reduction in UV–VIS parameters, and SRHA displayed an increase of 40% removal of all UV–VIS parameters. However, UV–VIS parameters expressed different attractions to the LF surface, color-forming moieties being preferentially adsorbed (54%) onto LF in comparison to UV-absorbing centers (38%) of SRFA. However, in the presence of *E. coli*, the adsorption extent decreased to 24–37% for SRNOM and 12–40% for SRHA and preferential adsorption of color-forming moieties in comparison to UV-absorbing centers of SRFA was observed. It should also be emphasized that the release of EPS from *E. coli* affected the adsorption extents under all conditions. Considering the sole effect of NOM analogue compounds on *E. coli* inactivation upon solar simulated irradiation conditions, protection from photoinactivation was reported in an HA range of 1–50 mg/L [25].

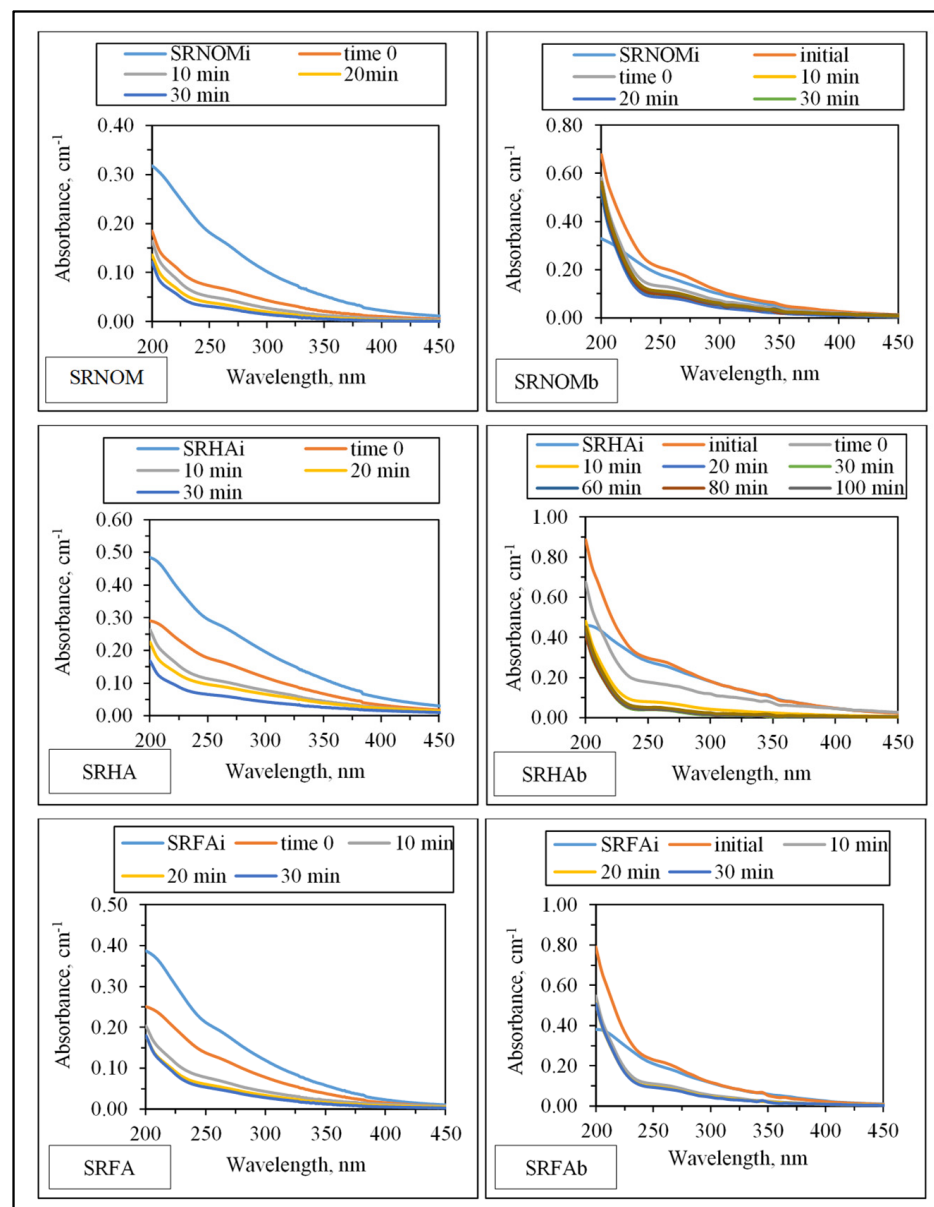


Figure 3. UV-VIS absorption spectral features of the organic matrix upon solar photocatalytic degradation of NOM compounds in the absence/presence of *E. coli* (b denotes the presence of bacteria).

Insignificant absorbance values for $\lambda > 400$ nm indicated the absence of chromophoric groups (color-forming moieties) related to the presence of systems including conjugated double bonds, aromatic rings, and phenolic functional groups containing atoms with lone pairs of electrons. Initial conditions revealed the release of organics expressing a shoulder in the 240–280 nm wavelength range. Absorbance values at $\lambda = 280$ nm were not significantly different from SRNOM_i, SRHA_i, and SRFA_i. However, in the UV range of $\lambda > 250$ nm, a sharp absorbance increase was evident under all conditions irrespective of NOM type. Upon introduction of LF to the suspension composed of *E. coli* and NOM compounds, the overall effect of surface interactions could be assessed by decreased absorbance values. The resultant organic matrix and *E. coli* cells were further subjected to solar photocatalysis. Following initiation of light exposure, a time-dependent decrease in absorbance was recorded in all spectral wavelength ranges.

For the assessment of specified UV-VIS parameters, irradiation-time-dependent removal profiles in the absence/presence of *E. coli* using NOM analogues were addressed in Figure 4. Prior to evaluation of solar photocatalytic removal efficiencies of specified

UV–VIS parameters, initial adsorption percentages were calculated to understand the surface coverage of LF in the absence/presence of *E. coli*. Upon instantaneous adsorption onto LF, UV₂₅₄ adsorption percentages were reduced from 60% to 36% for SRNOM and from 35% to 5% for SRFA, and no change was observed for SRHA. Regarding effective sizes of system variables, LF is expected to be adsorbed on *E. coli* cells through electrostatic interactions, whereas NOM analogues would have a tendency to be adsorbed onto LF, which was already adsorbed on bacterial cells. Consequently, the reduction in the surface coverage of LF particles could be attributed to occupying available sites of LF by *E. coli* cells, therefore reducing the interactions between active sites of the LF catalyst and NOM compounds [26,27].

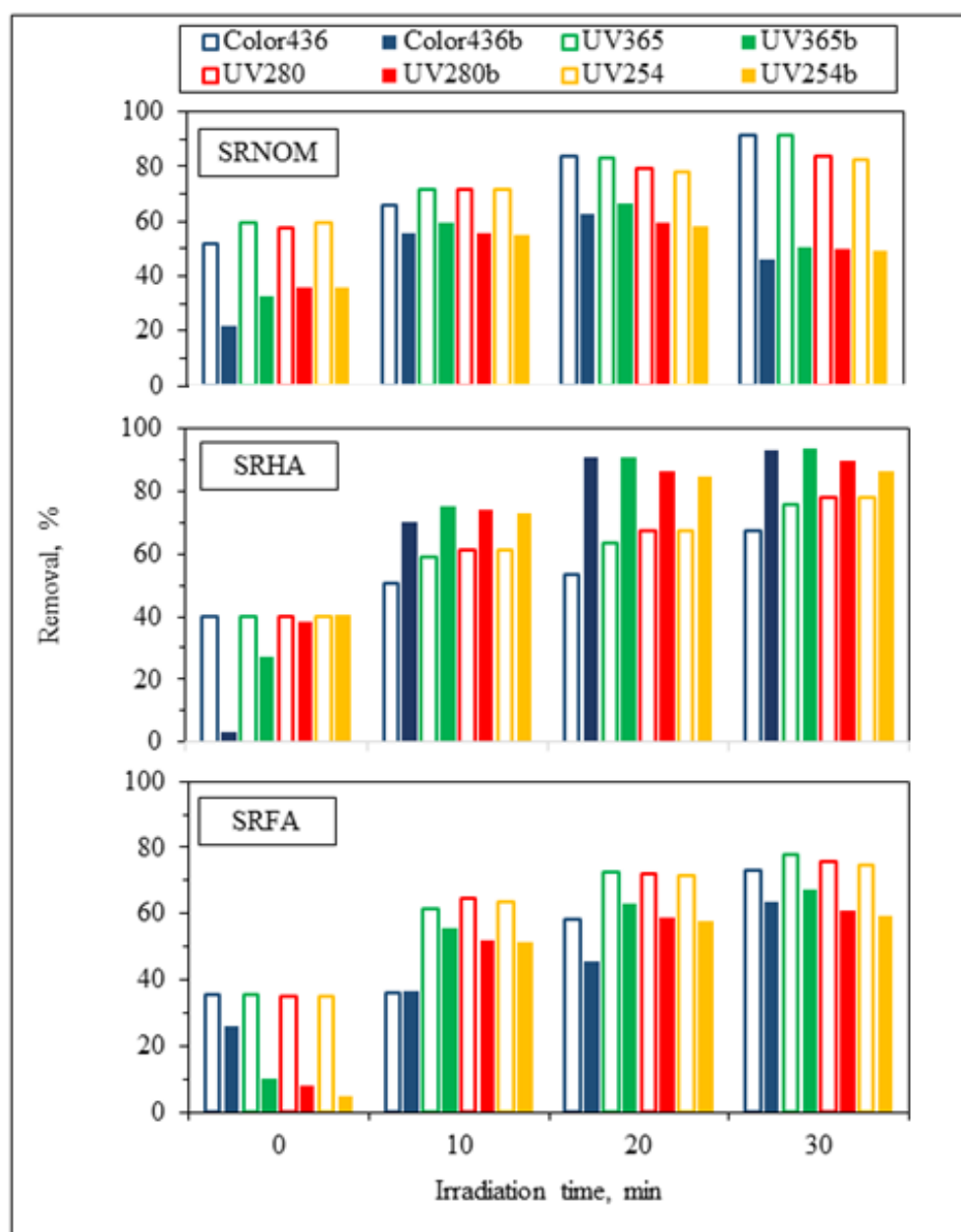


Figure 4. Irradiation-time-dependent removal profiles of specified UV–VIS parameters of the organic matrix upon solar photocatalytic degradation of NOM compounds in the absence/presence of *E. coli* (b denotes the presence of bacteria).

Following an irradiation period of 30 min, UV₂₅₄ removal efficiencies were reduced from 83% to 49% for SRNOM and from 75% to 59% for SRFA, whereas in the presence of

SRHA, the UV_{254} removal efficiency showed enhancement from 78% to 86%, indicating that the presence of *E. coli* significantly affects the overall removal efficiency of aromatic content either as enhancement or as diminution. In the presence of both *E. coli* and NOM analogues, UV_{254} removal efficiencies of organic matrices were revealed in decreasing order as SRHA > SRFA > SRNOM. The reason could be attributed to the aromatic content of NOM analogues, which has a strong effect on light transmission as well as energy consumption from UVC and solar irradiation [28]. Enhancement of the removal of specified UV–VIS parameters in the presence of SRHA could be related to its higher degree of aromaticity, as expressed by the $SUVA_{254}$ value (7.27 L/mg m), in comparison to SRNOM (4.18 L/mg m) and SRFA (4.53 L/mg m) (Table S1).

Further evaluation of changes in organic matrices upon solar photocatalytic degradation of NOM compounds in the absence/presence of *E. coli* was assessed in terms of irradiation-time-dependent changes in DOC contents, as presented in Figure 5.

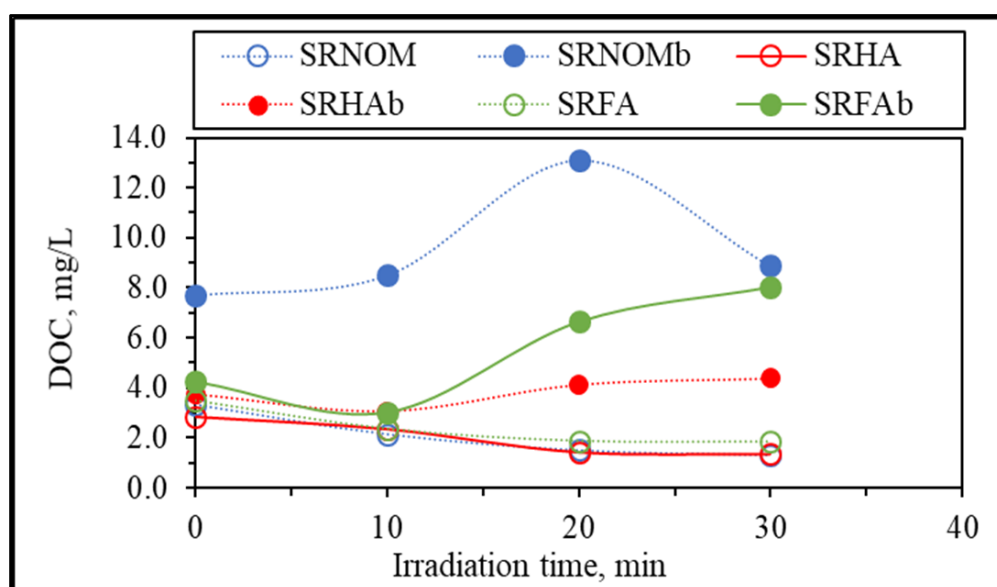


Figure 5. Irradiation-time-dependent DOC content of the organic matrix of samples upon solar photocatalytic degradation in the absence/presence of *E. coli* (b denotes the presence of bacteria).

Upon exposure to the solar photocatalytic degradation process, NOM representatives expressed a humic-like exponential decay profile for the DOC content with respect to increasing irradiation periods [29]. In contrast, the presence of *E. coli* displayed variations in DOC contents with respect to irradiation time, especially following $t_{irr} = 20$ min, which could be attributed to the release of cell components via the attack of reactive species on the cells. Upon destruction of bacterial cells, the release of aromatic proteins, such as tryptophan, tyrosine, and phenylalanine, as well as carbohydrates, contributes to the overall organic composition and therefore increases the DOC content, because these components can be retained in the reaction medium even after filtration through a $0.45 \mu\text{m}$ filter [30,31]. In the presence of SRHA and SRFA, a 2-log reduction in the bacterial count was achieved following $t_{irr} = 30$ min, which led to the release of cell components that ended up with an increase in the total organic carbon content, whereas for the same irradiation period and in the presence of SRNOM, a noticeable reduction in the overall DOC content was observed. The reason could be the bacterial inactivation profile in the presence of SRNOM, which revealed a shoulder between $t_{irr} = 20$ min and 30 min, indicating that the primary reaction is addressed to solar photocatalytic degradation of SRNOM and/or cell-released organics in NOM-initiated reactions instead of bacterial cell destruction.

Additional elucidation of the system was directed to specific UV–VIS absorbance ($SUVA$, L/mg m) parameters named $SUVA_{254}$ and $SUVA_{280}$, which are defined as the DOC normalized values of UV–VIS absorbance values at 254 nm and 280 nm and explained

successive removal of UV–VIS parameters in accordance with DOC contents (Figure 6). Since insignificant release of color-forming moieties was obtained in comparison to UV-absorbing centers, only $SUVA_{280}$ and $SUVA_{254}$ were presented.

It could be deduced from specific UV parameters that upon an irradiation period of 30 min, specified UV parameters and DOC were removed simultaneously, being more significant for SRFA and SRHA. However, SRNOM expressed a slight increase followed by a decreasing order with respect to increasing exposure times. Nevertheless, since all of the specific UV parameters were less than 4, the organic matrix could be considered as expressing mostly an aliphatic character lacking color-forming chromophoric centers. Upon further exposure ($t_{irr} > 30$ min), a steady trend was observed that could be ascribed either to a slow removal of both counterparts or to insignificant release of recalcitrant non-UV-absorbing organics.

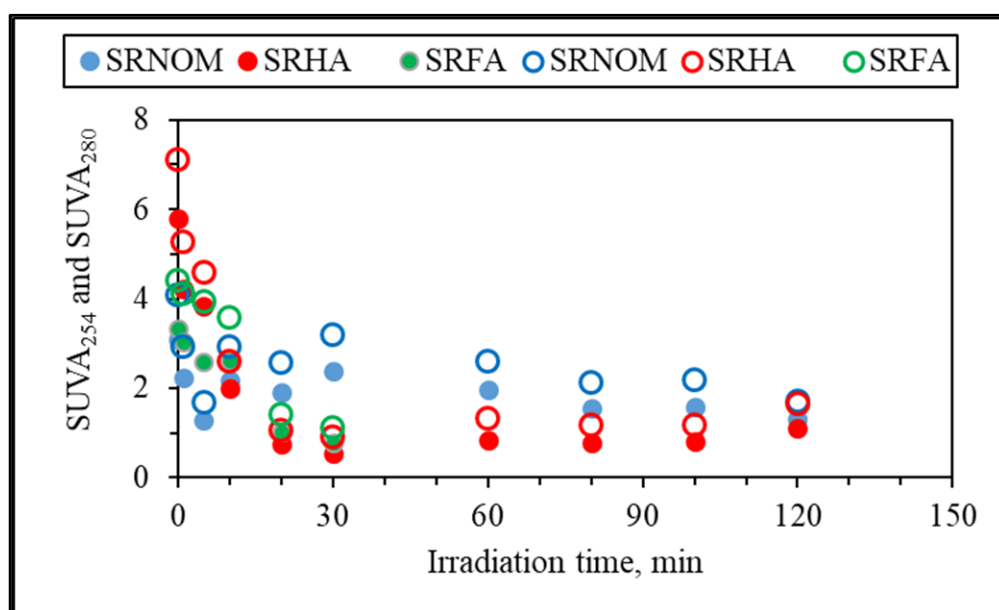


Figure 6. Specific UV parameters of the organic matrix released from *E. coli* inactivation in the presence of NOM analogue compounds. Closed circles represent $SUVA_{280}$, and open circles represent $SUVA_{254}$.

Synchronous scan fluorescence spectral features (indicated as synchronous scan fluorescence intensity, Fl_{sync}) of the organic matrix expressed irradiation-time-dependent variations with respect to the NOM analogue type (Figure 7).

Emergence of fluorophoric centers was more pronounced in the presence of SRNOM comparison with SRHA and SRFA. Fluorescence intensity profiles presented a broad distribution in the emission wavelength range of 250–500 nm. However, SRHA expressed more ordered fluorescence spectra with a well-defined peak at $\lambda = 280$ nm and a rather broad peak at $\lambda = 375$ nm. Synchronous scan fluorescence spectra of SRFA resembled those of SRNOM, with a peak at $\lambda = 280$ nm accompanied by broad fluorophoric regions in the longer-wavelength region. Complete removal of all fluorophores was not observed in accordance with UV–VIS spectral features as well as DOC contents; however, *E. coli* cells were almost completely removed ($<10^2$ CFU/mL) upon an irradiation period of 30 min. The underlying photochemical and photocatalytic reactions taking place in the presence of *E. coli* and NOM compounds were presented in SI.

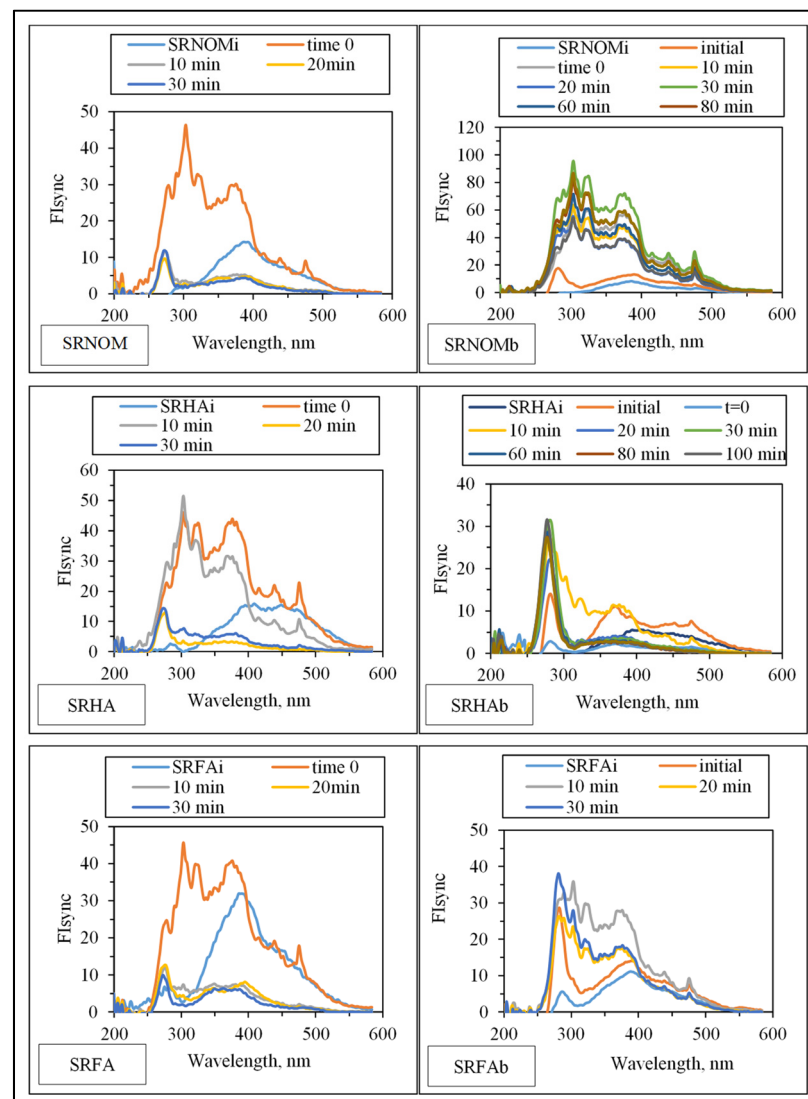


Figure 7. Synchronous scan fluorescence spectral features of the organic matrix upon solar photocatalytic degradation of NOM compounds in the absence/presence of *E. coli* (b denotes bacteria).

3.1.2.2. EEM Fluorescence Features in Combination with PARAFAC Modeling

Discrimination of organic matrix components originating from either degradation of NOM or destruction of *E. coli* would provide further information about the behavior of these individual components with their own environmental significance. The excitation and emission maxima values of the components (C1, C2, C3, and C4) determined by the PARAFAC model (Figure 8) were compared with related studies in order to classify fluorescence components derived from the SPCI of *E. coli* in the absence/presence of NOM compounds. Four fluorescent components were successfully decomposed by PARAFAC modeling in the EEM data set of 70 samples, including the SPCI of *E. coli* in the absence/presence of NOM using LF. To obtain further insight into the effect of NOM analogues, PARAFAC modeling was performed for three conditions: (i) samples in the absence of NOM, (ii) samples in the presence of NOM, and (iii) samples including conditions i and ii. The samples in the absence of NOM analogue compounds were compiled from a previous study reported by Birben et al. [6]. PARAFAC modeling may give different outcomes with respect to the samples defined in the beginning of the model, and to represent this situation, the authors ran the PARAFAC model three times with different sample inputs: (i) comprises EEMs of *E. coli* inactivation in the absence of NOM (SS, DW, MQ, WM), (ii) comprises EEMs of *E. coli* inactivation in the presence of NOM representatives

(SRNOM, SRHA, and SRFA), and (iii) comprises both samples from i and ii. Modeling i. and ii together (which is basically iii) aimed to show the shielding effect of humic-like fluorophores for the visualization of protein-like fluorophores.

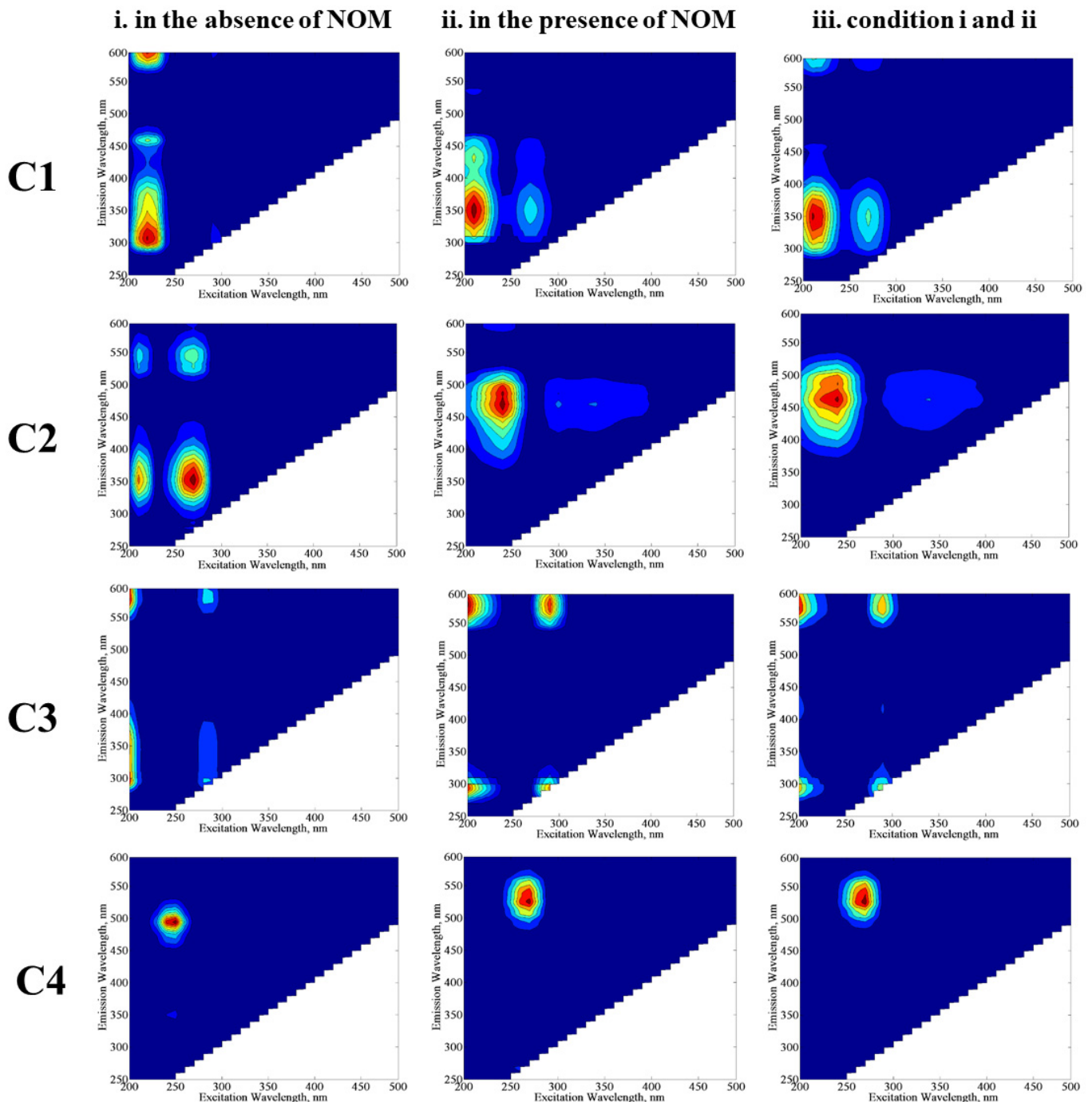


Figure 8. PARAFAC model output displaying four fluorescent components derived from the SPCI of *E. coli* in the absence/presence of NOM using LF.

In the absence of NOM compounds, component 1 (C1) displayed two peaks at $Ex/Em = 210/300$ nm and $210/460$ nm, which are related to protein/polyphenol-like components; more specifically, C1 could be regarded as a tryptophan-like fluorescent component [32–35]. In the presence of NOM compounds, C1 displayed two peaks at $Ex/Em = 210/350$ nm and $210/380$ nm, which also corresponds to protein/polyphenol-like components. When PARAFAC modeling was run by using all data for conditions i and ii,

C1 expressed two maxima at Ex/Em = 210/350 nm, and this component was also classified as a protein/polyphenol-like component. Although the absence and/or presence of NOM seems to cause an insignificant difference in the classification of C1 by PARAFAC modeling, peak positions for the emission wavelength displayed differences in the absence/presence of NOM, which could be attributed to the higher degree of aromaticity related to NOM.

Component 2 (C2) exhibited one primary maxima at Ex/Em = 250/450 nm, referring to a microbially derived fulvic-like or humic-like component of NOM released from degradation of microorganisms [36–38]. The presence of C1 and C2 strongly indicated that solar photocatalytic decay of *E. coli* or release of their cell organic matter is likely the source of fluorophoric components resembling natural waters. Component 3 (C3) revealed one maxima at Ex/Em = 245/475 nm for conditions ii and iii, whereas this component almost displayed no maxima for condition i. The reason could be attributed to the relevance of C3 to NOM-related reaction matrices. Component 4 (C4) showed one maxima at Ex/Em = 250/500 nm for condition i, whereas the Ex/Em maxima shifted to 260/525 nm for conditions ii and iii. In a similar manner achieved for C1, a shift of the Ex/Em maxima of C3 in the presence of NOM could be attributed to its higher aromaticity as well as molecular weight, causing a masking effect on the fluorescence features of bacteria-derived organics. Both C3 and C4 were identified as humic-like components [39–41].

Expressing fluorescence maxima at longer emission wavelengths, i.e., Em > 450 nm, C3 and C4 revealed humic-like component characteristics with a higher degree of aromaticity and a high molecular weight [33,35,37]. Depending on their fluorescence maxima values, the components presented molecular weights in the order of C3 > C4 > C2 > C1.

Although half of the experimental studies were performed in the absence of NOM, the PARAFAC model identified two different humic-like components with a highly aromatic structure and a higher molecular weight. The reason of the occurrence of this humic-like fluorescence could be attributed to a hypothetical abiotic condensation process by which carbohydrates and amino acids can produce compounds with a melanin structure [42]. It was previously reported that this type of reaction may occur between carbohydrates and proteins released by bacteria [43]. With respect to the experimental data of this study, it has been reported that the SPCI of *E. coli* ends up with the release of carbohydrates and proteins via cell lysis; therefore, the condensation reaction between these compounds could be the source of humic-like components identified by the PARAFAC model. In addition, another plausible explanation of humic-like fluorescent components could be auto-oxidative crosslinking of unsaturated lipids released by organisms [44,45]. To perform a further assessment of the fate of individual PARAFAC components following solar photocatalysis, changes in the Fmax values of each component under all experimental conditions are presented in Figure 9. Fluorescent components identified by EEM/PARAFAC have distinct excitation and emission spectra. However, identified components may represent a single fluorophore or a group of similar fluorophores. Once identification of the components explaining the greatest variation proceeded, calculation of the distribution of components could be performed for each sample. PARAFAC modeling could make quantitative determination of an analyte possible by adding a known amount of this analyte for the determination of its concentration in each sample. Otherwise for an unknown PARAFAC component, it is impossible to convert fluorescence intensities to concentration values. Therefore, the maximum fluorescence intensities (Fmax) of the identified DOM components were used as the representative of the relative proportions of the components. Fmax is derived by multiplying the maximum excitation and maximum emission loading for each component by its score, which produces intensities in the same measurement scale as the original EEMs.

For comparison, changes in the normalized Fmax (F_{\max_t}/F_{\max_j}) intensities of each component were presented for an irradiation period of 60 min in the absence/presence of NOM (Figure 10).

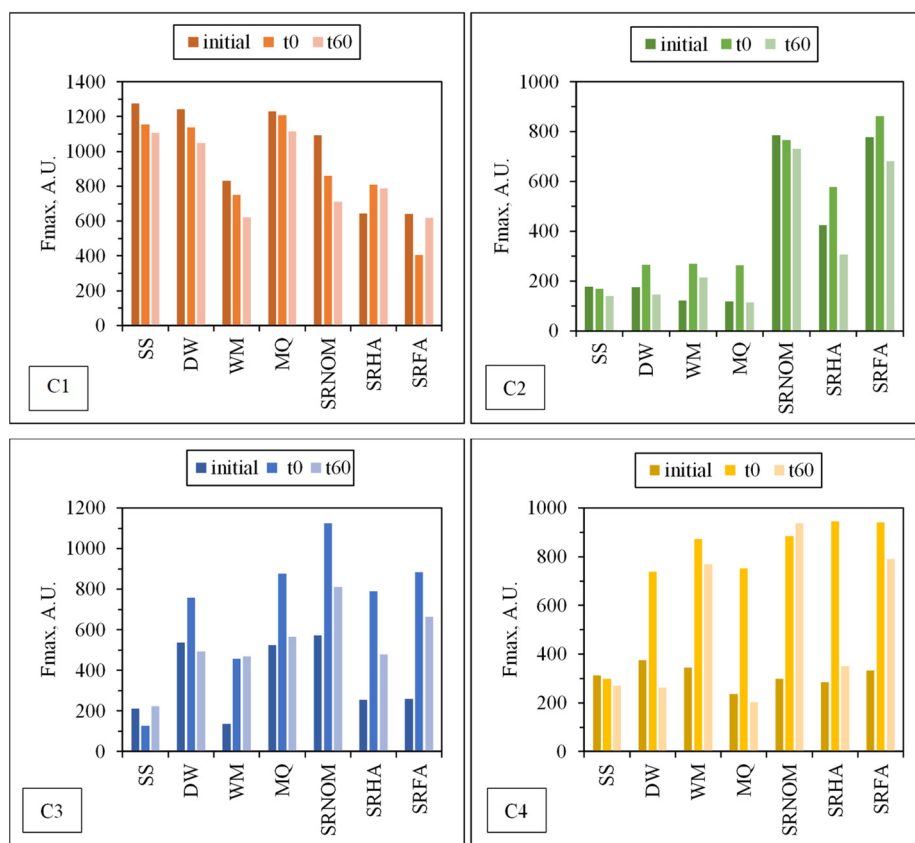


Figure 9. Changes in Fmax values of individual PARAFAC components prior to and following solar photocatalysis under all experimental conditions.

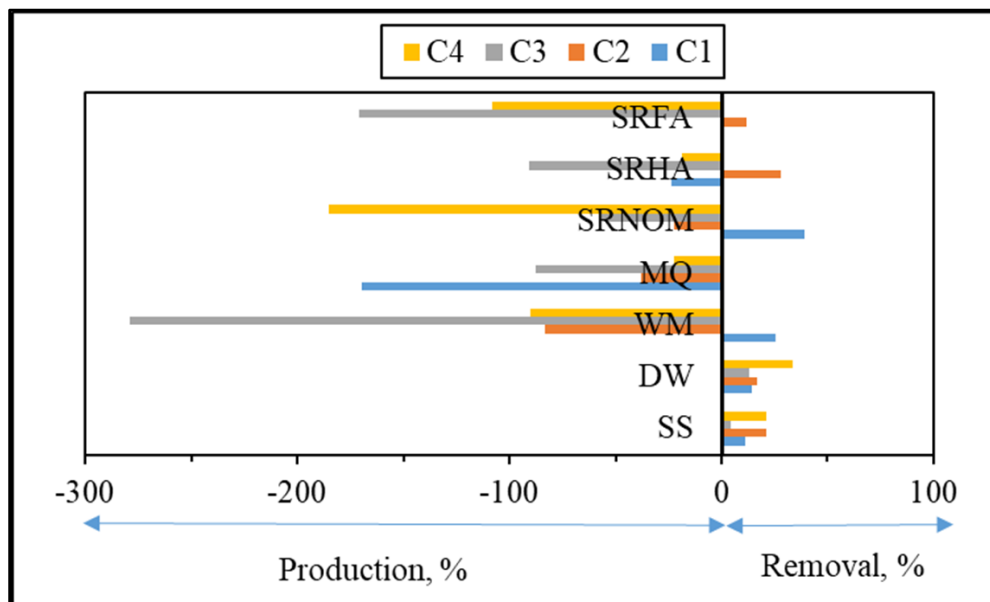


Figure 10. Changes in normalized Fmax values of PARAFAC components upon the SPCI of *E. coli* in the absence/presence of NOM using LF ($t_{irr} = 60$ min).

Upon exposure to SPCI for $t_{irr} = 60$ min, C1 removal efficiencies were found to be 11% for SS, 14% for DW, 26% for WM, and 39% for SRNOM, whereas a 170% increase was attained in the presence of MQ, and 24% and 1% increases were achieved for SRHA and SRFA, respectively. It has been previously reported that solar photocatalytic degradation

of proteins could be expected as a result of ROS attack on the aromatic ring of tryptophan-like proteins [46,47]. Removal of the protein-like component (C1) was observed in the presence of SS, DW, WM, and MQ; however, an increase in C1 (18%) and irrelevant removal (< 5%) of C1 were attained in the presence of SRHA and SRFA, which could be attributed to the competitive reactions between humic matter and protein-like components for ROS. Moreover, since SPCI is also continuing, bacteria-derived organics are also released concomitantly via cell lysis. Consequently, competitors for ROS are bacteria, bacteria-derived organics, and NOM in the presence of SRNOM, SRHA, and SRFA.

The most noticeable increase was observed for C3 and C4 in the presence of WM, SRNOM, SRHA, and SRFA, whereas under the same experimental conditions, removal of these fluorophores could be observed in the presence of SS and DW. The reason could be the emergence of these fluorophores only after the SPCI of *E. coli*, followed by solar photocatalytic degradation of these in situ generated fluorophores. However, in the presence of NOM, various reactions could occur, such as (i) the SPCI of *E. coli*; (ii) solar photocatalytic degradation of NOM; (iii) solar photocatalytic degradation of *E. coli*-derived organics, i.e., proteins and carbohydrates; and (iv) reactions between degraded and/or non-degraded fractions of NOM and bacteria-derived organics. Although C3 and C4 were regarded as fluorescent components with a higher molecular weight and aromaticity, their normalized Fmax values indicated the formation of these fluorophores under the specified conditions. As a result of SPCI, bacteria-derived organics would be released into the reaction medium due to cell lysis, while degradation of humic matter could also proceed concomitantly. Consequently, condensation reactions between bacteria-derived organics as well as humic fractions could be expected, which then generates high-molecular-weight fluorescence components, such as C3 and C4.

3.1.2.3. FTIR Spectroscopy

Since the main purpose was to elucidate FTIR spectral features of the complex reaction medium prior to and following the SPCI of *E. coli* in the absence/presence of organic matter, emphasis was given primarily to the band positions rather than band intensities.

In general, an IR absorption spectrum of bacteria is divided into five major areas:

Area 1 (~3000–2800 cm⁻¹): commonly dominated by C-H stretching of fatty acid compounds related to lipid content

Area 2 (~1700–1500 cm⁻¹): dominated by proteins

Area 3 (~1450–1200 cm⁻¹): a mixed region dominated by the carboxylic groups of proteins, free amino acids, and polysaccharides (1450–1400 cm⁻¹), and RNA/DNA and phospholipids (1250–1200 cm⁻¹)

Area 4 (~1200–900 cm⁻¹): dominated by polysaccharides

Area 5 (<900 cm⁻¹): the fingerprint region containing bands that cannot be assigned to specific functional groups

FTIR spectral bands attributed to the main organic components of *E. coli* both as solely and following irradiation upon the use of TiO₂ have been assessed in detail by Kiwi et al. [48–50]. With respect to the above-given major windows and the data reported by Kiwi et al., the peaks related to the main components of the cell wall of *E. coli* as the LPS content, phospholipid bilayer, and peptidoglycan layer were compiled and presented in Table S3 in the SI section. In accordance with these bands, the following descriptive variations were observed under the specified experimental conditions. For comparison purposes, the samples originating from the experimental study performed in the absence of organic matter were also subjected to FTIR analyses. All FTIR data were evaluated with respect to spectral properties observed in both transmission mode (Figures 11 and 12) as well as second-derivative mode (Figures S3 and S4). Designated wavenumbers were mostly derived from both spectral features, and fingerprint regions were presented.

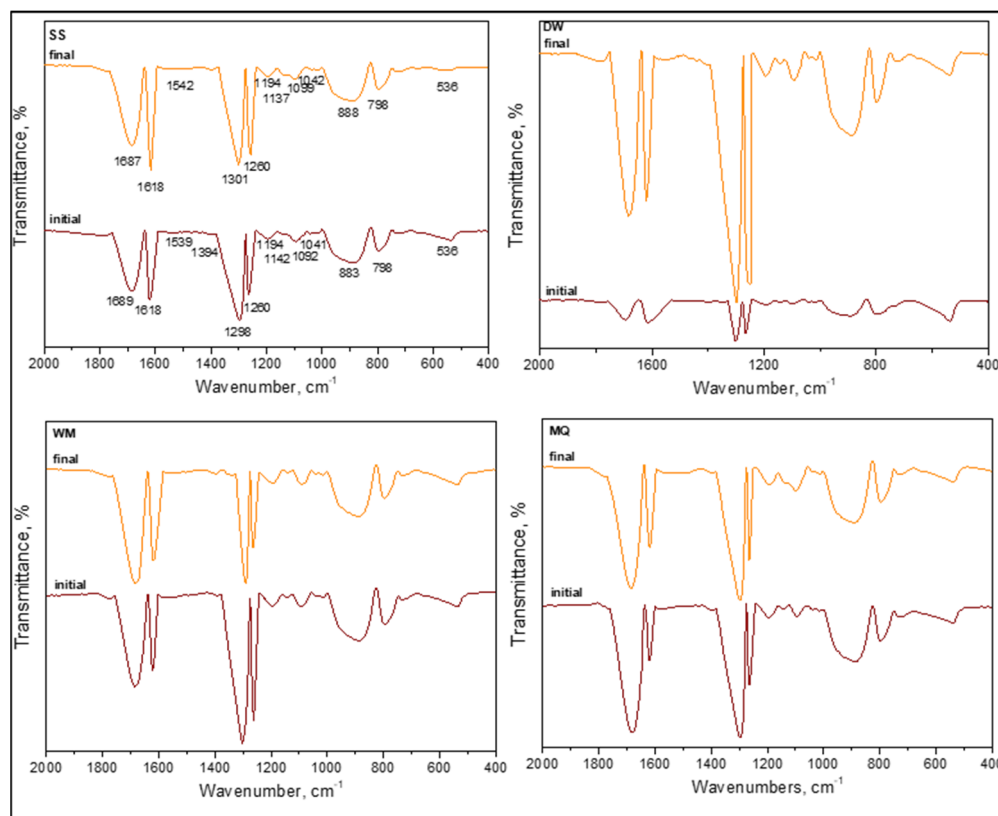


Figure 11. FTIR transmittance spectra of *E. coli* and LF under various conditions in the absence of NOM compounds prior to (initial) and following (final) SPCI.

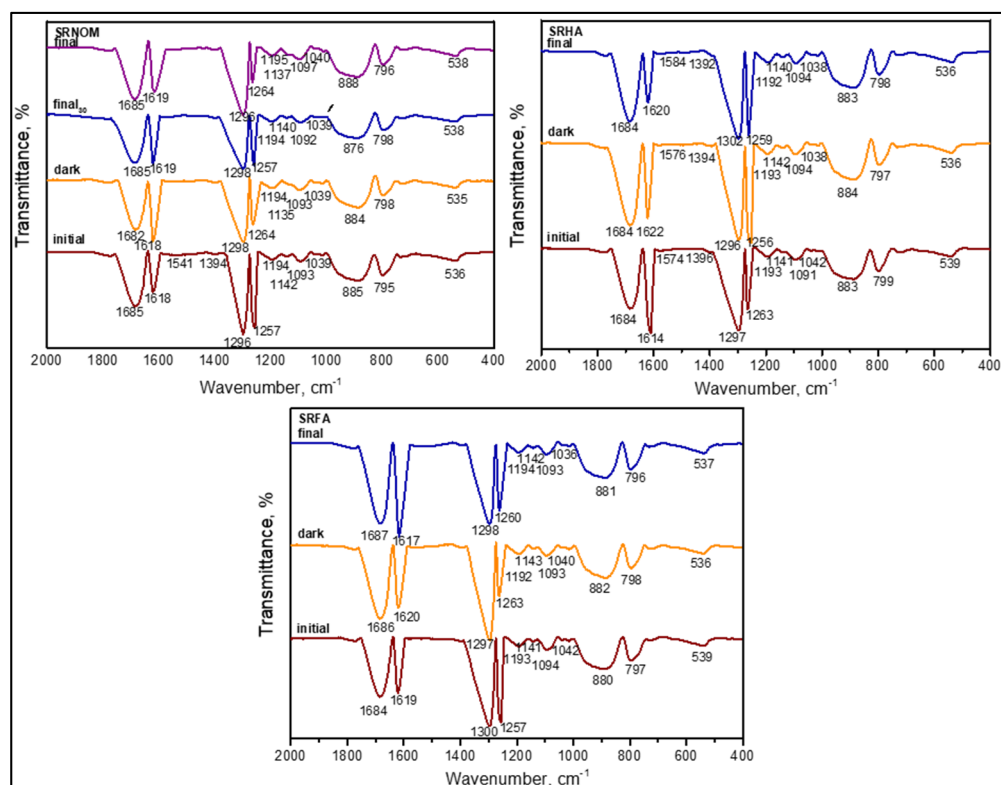


Figure 12. FTIR transmittance spectra of *E. coli* and LF in the presence of NOM compounds prior to (initial) and following (final) SPCI.

3.1.2.4. FTIR Spectral Features of *E. coli* in the Absence of Organic Matter

In the absence of organic matter, the SPCI of *E. coli* was followed under various aqueous medium conditions, i.e., SS, DW, WM, and MQ [6]. The samples were designated as (i) initial ($t = 0$ condition) and (ii) final following SPCI for an irradiation period of 60 min. From a general perspective, all samples displayed the existence of organics upon introduction of LF and were produced in situ during 0.45 μm membrane filtration (Figure 11). Slight shifts were recorded in all specific regions most probably due to the masking effect of the solution matrix on the possible interactions between the species.

Contrary to the absence of amide A ($\nu 3300\text{ cm}^{-1}$) and amide B ($\nu 3100\text{ cm}^{-1}$) bands of NH stretching, the presence of amide I ($\nu 1700\text{--}1600\text{ cm}^{-1}$), amide II ($\nu 1600\text{--}1500\text{ cm}^{-1}$), and amide III (around $\nu 1290\text{--}1280\text{ cm}^{-1}$) bands were evident under all conditions irrespective of the solution matrix composition. These peaks were related to peptide bonds, and as the major protein band, the amide I band was mainly associated with the C=O and C–N stretching vibrations, whereas amide II represented mainly in-plane N–H bending and C–N and C–C stretching vibrations. Furthermore, amide IV–VII bands in region $\nu 750\text{--}200\text{ cm}^{-1}$ were not considered due to the complexity of identification. Excluding the slight shifts in peak positions, their presence under both initial and final conditions expressed the resistance of these organic fractions to SPCI using LF.

The presence of lipids designating the cell wall destruction were expected in the $\nu 2950\text{--}2840\text{ cm}^{-1}$ region mainly described as asymmetric and symmetric aliphatic C–H stretching vibrations of CH_3 and CH_2 groups and around the $\nu 1740\text{ cm}^{-1}$ region related to C=O stretching of carbonyl vibrations present in triglycerides. All samples displayed the aforementioned peaks with slight shifts under both initial and final conditions, being not affected by the solution properties.

Referring to the peaks of carbohydrates that were expected in the region of $\nu 1200\text{--}950\text{ cm}^{-1}$, designating the sugar rings of LPS as $\nu 1170\text{ cm}^{-1}$ related to the C–O stretching, $\nu 1120\text{--}1140\text{ cm}^{-1}$ as the asymmetric C–O–C stretching vibration band of glycosidic linkages, and $\nu 1060\text{--}1040\text{ cm}^{-1}$ as symmetric $\delta(\text{COH})$ stretching vibration of carbohydrates, all samples exhibited slight shifts with respect to the components present in the solution matrix. Since no difference was observed between the FTIR spectral features of initial and final samples, the continuous removal and emergence of the specified groups could be visualized. Asymmetric and symmetric phosphate (PO_2^-) stretching vibrations of the nucleic acid detected at $\nu 1280\text{--}1200\text{ cm}^{-1}$ and the symmetric PO_2^- band of DNA at $\nu 1085\text{ cm}^{-1}$ were present with slight shifts in all samples referred to as initial and final under all conditions. Contrary to the findings of Kiwi et al., it should also be mentioned that neither the $\delta(\text{CH}_2)$ scissor ($\nu 1470\text{ cm}^{-1}$) nor $-\text{COO}^-$ ($\sim \nu 1400\text{ cm}^{-1}$) stretching bands were detected. In a similar manner, the $\nu 1575\text{ cm}^{-1}$ band related to aspartate or glutamate carboxylate stretching was not observed. Under all conditions and irrespective of the reaction medium properties, $\nu 1620\text{ cm}^{-1}$ represented H–O stretching vibration related to water absorption. The band at around $\nu 1390\text{ cm}^{-1}$ could be attributed to the presence of NO_3^- in WM medium that was detected following solar photocatalysis contrary to the insignificant contribution under the initial condition most probably due to the attractive electrostatic interactions toward the positively charged LF surface. Considering out-of-plane bending of aromatic C–H in the $\nu 975\text{--}775\text{ cm}^{-1}$ region and asymmetric C–N stretching at $\nu 966\text{ cm}^{-1}$, specific interest should be directed to LF. In all samples, the presence of LF could be detected by the peaks of Fe–O and O–Fe–O stretching bonds at around $\nu 850\text{ cm}^{-1}$ and Fe–O stretching of FeO_6 octahedron groups at $\nu 560\text{ cm}^{-1}$ [51]. Contrary to XPS verification, the absence of the $\nu 1490\text{--}1382\text{ cm}^{-1}$ band related to the splitting of the asymmetric stretching of metal carbonates and the $\nu 425\text{ cm}^{-1}$ band due to Fe–O–Fe bending or deformation modes should also be mentioned [7].

Bearing in mind the variations in selected aqueous medium compositions, MQ expressed the immediate burst out due to osmotic pressure followed by DW that could also be related to limited survival conditions. However, the presence of WM components expressed a decreasing intensity profile upon irradiation in comparison to the initial condition, most probably due to competing inorganic–organic reactions resulting in both band positions and relative intensities.

Interestingly, no significant correlation could be visualized with reaction kinetics [6] and FTIR spectral features emphasizing the non-selective oxidation mechanism of solar photocatalysis. However, with respect to UV-VIS and fluorescence spectral properties, the resistance of DNA groups to ROS-mediated solar photocatalysis was evidenced by FTIR spectra [52].

It should also be mentioned that FTIR data were limited to a selected irradiation period, and therefore, possible detection of the remaining *E. coli* cells as well as organics could be achieved. Therefore, elucidation of FTIR peaks upon the SPCI of *E. coli* using LF should only be considered under a qualitative basis rather than related to kinetics of simultaneously operating inactivation and degradation. More significantly, the effect of the aqueous solution composition was found to be weak on the band positions exhibiting slight shifts, although relatively minor variations were detected in intensities.

3.1.2.5. FTIR Spectral Features of *E. coli* in the Presence of Organic Matter

The SPCI of *E. coli* was followed under various aqueous medium conditions consisting of organic matter such as SRNOM, SRHA, and SRFA. All samples were considered in the presence of LF. As indicated above, the expected vibrational bands (cm^{-1}) of the functional groups are presented in Table S3 in SI. In a similar manner, the samples were designated as (i) initial and (ii) final, following SPCI. From a general perspective, all samples displayed the existence of functional groups ascribed to both humic substances as well as *E. coli* both prior to and following SPCI (Figure 12).

SRNOM as a heterogeneous polydisperse organic matrix mainly composed of both humic and fulvic acids displayed the absence of bands in the region of $\nu 3400\text{--}3600\text{ cm}^{-1}$ that were associated with O-H stretching (alcohols, phenols, and carboxylic groups), N-H stretching (trace/minor), and hydrogen-bonded OH groups. However, upon enlargement of the spectra, a weak broad band at $\sim\nu 3100\text{ cm}^{-1}$ related to amide B bands of N-H stretching-vibration-related amide II groups could be visualized. In contrast, amide I groups in the $\nu 1760\text{--}1600\text{ cm}^{-1}$ region related to C=O and C-N stretching vibrations could also be noticed under all conditions, even upon prolonged dark interactions ($t_{\text{irr}} = 30$ min) and during SPCI for irradiation periods of 30 min and 60 min. Apart from the slight shifts in peak positions, their presence under both initial and final conditions showed the resistance of these organic fractions to SPCI using LF. It should be indicated that these carbonyl vibrations could be concurrently related to both the presence of triglycerides originating from *E. coli* and/or the humic organic core.

The absence of a vibrational band at $\nu 1660\text{--}1630\text{ cm}^{-1}$ of C=O of quinone and/or H-bonded conjugated ketones and $\nu 1620\text{--}1600\text{ cm}^{-1}$ referring to aromatic C=C skeletal vibrations and COO^- symmetric stretching could be correlated to the organic matrix filtered, as evidenced by UV-VIS and synchronous scan fluorescence spectroscopic features (Figures 3 and 7).

As denoted by the presence of lipids indicating cell wall destruction, vibrations in the $\nu 2950\text{--}2840\text{ cm}^{-1}$ region of asymmetric and symmetric aliphatic C-H stretching vibrations of CH_3 and CH_2 groups were evidently noticed expressing resistance to degradation via solar photocatalytic oxidation. In contrast, carbohydrate peaks expected in the region of $\nu 1200\text{--}950\text{ cm}^{-1}$ designating the sugar rings of LPS as $\nu 1170\text{ cm}^{-1}$ related to the C-O stretching, $\nu 1120\text{--}1140\text{ cm}^{-1}$ as the asymmetric C-O-C stretching vibration band of glycosidic linkages, and $\nu 1060\text{--}1040\text{ cm}^{-1}$ as symmetric $\delta(\text{COH})$ stretching vibration of carbohydrates, all samples exhibited slight shifts with respect to the components present in the solution matrix. However, no difference was observed between initial and final samples, indicating that during SPCI, the disappearance and emergence of these groups were expected, as verified by both DOC contents and specified spectral properties.

Asymmetric and symmetric PO_2^- stretching vibrations of the nucleic acid at $\nu 1280\text{--}1200\text{ cm}^{-1}$ and the symmetric PO_2^- band of DNA at $\nu 1085\text{ cm}^{-1}$ were present with slight shifts as $\nu 1257\text{--}1262\text{ cm}^{-1}$, as evidenced by both transmission and second-derivative spectral features. It should be indicated that the amide III band at $\nu 1290\text{--}1280\text{ cm}^{-1}$ expressing C-N stretching and N-H stretching could also

be demonstrated. Moreover, bands at $\nu 1260\text{--}1200\text{ cm}^{-1}$ of C-O stretching and OH deformation of COOH and C-O stretching of aryl ethers and phenols were detected. However, the absence of bands at $\nu 1385\text{--}1380\text{ cm}^{-1}$ of the symmetrical stretching of carboxylic groups could also be related to the organic matter composition of the solution passing through $0.45\text{ }\mu\text{m}$ membrane filters. Concurrently, these groups could also be used in surface interactions along with the bands in the region of $\nu 3400\text{--}3600\text{ cm}^{-1}$ that were associated with the O-H stretching of alcohols and carboxylic groups.

The aspartate or glutamate carboxylate stretching band at $\nu 1575\text{ cm}^{-1}$ was not observed, as evidenced by both protein contents and UV-VIS and synchronous scan fluorescence spectral features of the filtered samples (Figures 3 and 7).

In accordance with the SPCI of sole *E. coli* performed under various aqueous medium conditions, neither $\delta(\text{CH}_2)$ scissor ($\nu 1470\text{ cm}^{-1}$) stretching nor $-\text{COO}$ ($\sim\nu 1400\text{ cm}^{-1}$) asymmetric stretching bands were detected. The vibrational band at $\nu 1620\text{ cm}^{-1}$ of H-O stretching related to water absorption was clearly apparent under all experimental conditions. More specifically, out-of-plane bending of aromatic C-H groups at the vibrational band at $\nu 975\text{--}775\text{ cm}^{-1}$ was detected at around $\nu 795\text{--}800\text{ cm}^{-1}$ by transmission as well as via second-derivative spectra. Although expected in this band region as $\nu 996\text{ cm}^{-1}$, an asymmetric C-N stretching band was not observed.

The possible effects of SRHA and SRFA were directly compared to the FTIR spectral bands detected in the presence of SRNOM (Figure 12). Since SRHA was composed of a denser aromatic core and functional groups mainly composed of carboxylic and phenolic groups, similarities to SRNOM were expected. Although the major bands were almost similar, upon the SPCI of *E. coli*, slight variations in $\nu_a(\text{CH}_3)$, $\nu_a(\text{CH}_2)$, $\nu_s(\text{CH}_3)$, and $\nu_s(\text{CH}_2)$ band positions as well as shapes were visualized. The presence of SRFA exerted a similar effect with variations quite different in comparison to the FTIR spectral features attained in the presence of SRHA and SRNOM. Slight shifts were recorded in all specific regions most probably due to the masking effect of the organic solution matrix on the possible interactions between the species.

Excluding minor dissimilarities, the observed close proximities expressed the significant behavior of the specific organic matrix and *E. coli* system during solar photocatalysis. Due to the surface-oriented nature of the non-selective oxidation mechanism, continuously operating the removal and formation of organic fractions originating from either humic matter or *E. coli* destruction could result in an almost consistent presence of all vibrational bands.

It should also be mentioned that the FTIR data were limited to a selected irradiation period, enabling the possible detection of the remaining *E. coli* cells as well as determination of characteristic properties of the organics. Therefore, elucidation of FTIR peaks upon the SPCI of *E. coli* using LF should only be considered under a qualitative basis rather than related to kinetics of simultaneously operating inactivation and degradation.

It should be indicated that no complete mineralization was targeted. Direct discrimination was not focused on the FTIR spectra of sole *E. coli* and/or organic matter due to the expected complex reaction mechanism operating under irradiation in the presence of LF. Moreover, pH-dependent surface interactions prevailing both prior to and under irradiation during SPCI and varying size effects would strongly alter FTIR spectral features.

It should also be mentioned that organic matter should pass through $0.45\text{ }\mu\text{m}$ membrane filters due to the operational definition of DOC; therefore, FTIR spectra expected for solid samples would be erroneously interpreted [53].

3.1.3. Analytical Detection of Cellular Constituents Released upon SPCI

As the major inactivation products, release of K^+ ions and protein contents were presented in Figures 13 and 14.

As expected, quite few K^+ ions were present under initial conditions followed by almost a similar amount of K^+ that could be detected upon introduction of LF to the aqueous medium. It should also be kept in mind that both attractive as well as repulsive electrostatic interactions could take place simultaneously, resulting in an average of 0.419 mg/L . Fol-

lowing SPCI ($t_{irr} = 60$ min), due to destruction of cell walls, release of K^+ ions was expected along with a decrease in cell counts (Figure 1 and Table 1). Although slight variations could be attributed to the presence of various NOM analogue compounds, the decreasing order could be presented as SRNOM > SRFA > SRHA. Electrostatic surface interactions could play the major role in the assessment of K^+ ion contents due to the filtration step most probably causing co-adsorptive removal prior to analytical determinations.

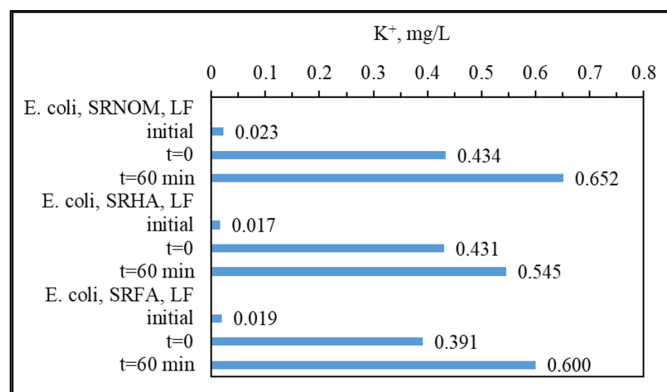


Figure 13. Change in K^+ content in the presence of NOM analogous prior to and following the SPCI of *E.coli* using LF.

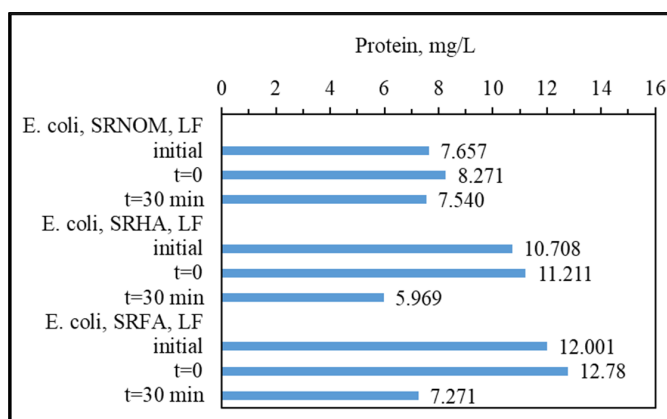


Figure 14. Protein contents of reaction matrices by the SPCI of *E. coli* in the presence of NOM analogues using LF.

Initial protein contents could be explained by the presence of EPS and organic matter composed of protein sub-units that are not significantly affected upon further introduction of LF for each NOM analogue compound. However, it was clearly evident that proteinaceous organic matter also underwent degradation during irradiation, as shown by lower contents. However, the presence of protein components could not be specifically designated by synchronous scan spectral features, although it could be assessed through both EEM fluorescence contour plots as well as PARAFAC model components.

Since PARAFAC component C1 refers to the protein-like fluorescent component, its F_{max} value would give information for the further evaluation of changes in the protein content of samples from a different point of view. For this purpose, the F_{max} values of C1 were plotted against the protein content of the samples, as determined by the Lowry method, and the data are presented in Figure S5 in SI. A significant correlation ($R^2 > 0.85$) between the protein content and the F_{max} values of C1 were attained prior to and following the SPCI of *E. coli* under different conditions excluding the WM effect. The reason could be attributed to the complexity of the WM due to the presence of common anions and cations with varying concentration values that affects photo-induced reactions (formation of anion-originated radicals) as well as ROS-related reactions (radical scavenging), making

the reaction mechanism unpredictable. Therefore, evaluation of the SPCI mechanism in the presence of natural water matrix components creates complexity and should be cautiously interpreted via alternative methods.

4. Conclusions

In this study, the SPCI of *E. coli*, in the presence of various NOM analogue compounds, such as SRNOM, SRHA, and SRFA, was investigated using LF as the novel photocatalyst. In addition to UV–VIS and synchronous scan fluorescence spectroscopic analysis, mechanistic investigation of cell-derived organics was also presented. EEM fluorescence spectra with PARAFAC modeling revealed further information about the occurrence and/or disappearance of NOM-related fluorophores as well as bacteria-related fluorophores upon SPCI. Furthermore, FTIR analyses expressed alterations in functional groups originating from both removal and concurrent generation of organics, although noticeable *E. coli* destruction was attained.

Four individual fluorescent components (C1, C2, C3, and C4) were successfully decomposed by PARAFAC modeling on the EEM data set of samples, including SPCI of *E. coli* in the absence/presence of NOM using LF. Both bacteria-derived fluorophores and humic-related fluorophores were identified and quantified with corresponding Fmax values. Protein content and protein-like fluorophores identified by PARAFAC modeling revealed strong correlation ($R^2 > 0.85$) excluding the WM effect, indicating multi-assessment of same parameter with the contribution of different tools. However, since WM components are major constituents of natural water conditions and have a crucial impact on photo-induced reactions, interpretation of the SPCI mechanism under these conditions should be carefully followed. Consequently, EEM fluorescence features revealed qualitative assessment of humic-related and bacteria-related fluorophores, whereas EEM in combination with the PARAFAC model brought up deeper information about the behavior of individual PARAFAC components quantitatively under specified conditions.

As inactivation indicative parameters, K^+ leakage expressing cell wall destruction and protein release as components of the intra-cellular organic matrix were determined. However, the presence of NOM analogue compounds directly affected the analytical determinations through various experimental pathways (i.e., filtration), most significantly via electrostatic interactions. Consequently, the use of advanced techniques for the detection of cell-derived parameters should be cautiously interpreted in order to eliminate matrix effects that could be originated from real natural water samples.

As a conclusive remark, based on both previous reports [6,7] and the presented findings, it could be indicated that LF could be successfully applied as a multitask novel photocatalyst specimen either for sole inactivation of bacteria or for degradation of NOM. Moreover, both could also be simultaneously performed under natural water conditions for remediation purposes effectively.

Supplementary Materials: The following are available online at <https://www.mdpi.com/article/10.3390/w13192785/s1>, Figure S1: UV-vis and synchronous scan fluorescence spectral features of NOM compounds, Table S1: Specified and specific UV–VIS and fluorescence parameters of NOM compounds, Figure S2: EEM fluorescence spectral features of IHSS NOM compounds, Table S2: Acid functional groups of NOM compounds, Table S3: Fourier transform infrared spectroscopic bands related to *E. coli* and NOM, Figure S3: Second-derivative FTIR spectra of *E. coli* and LF under various conditions in the absence of NOM compounds prior to (initial) and following (final) SPCI, Figure S4: Second-derivative FTIR spectra of *E. coli* and LF under various conditions in the presence of NOM compounds prior to (initial) and following (final) SPCI, Figure S5: Correlation between Fmax values of PARAFAC component C1 and protein contents prior to and following solar photocatalytic inactivation of *E. coli* in the absence/presence of NOM.

Author Contributions: Conceptualization, M.B. and I.N.S.; methodology, N.C.B., N.T., M.B. and I.N.S.; validation, N.C.B., N.T., M.B. and I.N.S.; formal analysis, N.C.B., E.L., R.P. and N.T.; investigation, N.C.B., N.T., M.B. and I.N.S.; data curation, N.C.B., E.L. and N.T.; writing—original draft preparation, N.C.B., N.T., M.B. and I.N.S.; writing—review and editing, N.C.B., N.T., M.B. and I.N.S.;

visualization, N.C.B. and N.T.; supervision, M.B. and I.N.S.; project administration, M.B. and I.N.S. All authors have read and agreed to the published version of the manuscript.

Funding: The grant provided by the University of Bergamo, Department of Engineering and Applied Sciences, on May 2019 to Bekbolet as visiting professor is highly acknowledged. This cooperation brought significant contributions to the realization of the studies denoted by [6,7].

Institutional Review Board Statement: Not applicable.

Informed Consent Statement: Not applicable.

Data Availability Statement: The data presented in this study is available on request from the corresponding author.

Acknowledgments: The authors would also like to express their special thanks to C. Schmid and L. Cozzarini, Department of Engineering and Architecture, University of Trieste, Trieste, Italy, for their valuable contributions in understanding of FTIR data.

Conflicts of Interest: The authors declare no conflict of interest.

Abbreviations

| | |
|--------------------------------------|--|
| AOPs | Advanced oxidation processes |
| C1, C2, C3, and C4 | The excitation and emission maxima values of the components determined by PARAFAC model. |
| CFU | Colony forming units |
| DOC | Dissolved organic carbon |
| DW | Distilled/deionized water |
| <i>E. coli</i> | <i>Escherichia coli</i> |
| EEM | Excitation emission matrix |
| EPS | Extracellular polymeric substance |
| FA | Fulvic acid |
| Fmax | Maximum fluorescence intensity at PARAFAC modeling |
| Fmax _i /Fmax _i | Normalized Fmax intensities of each component. |
| ATR-FTIR | Fourier transform infrared spectroscopy equipped with an attenuated total reflection |
| HA | Humic acid |
| IHSS | International Humic Substances Society |
| LaFeO ₃ | LF |
| LPS | Lipopolysaccharide |
| MQ | MilliQ water, ultra pure water |
| NOM | Natural organic matter |
| NOM analogues | SRNOM, SRHA, and SRFA |
| PARAFAC | Fluorescence spectra with parallel factor multiway analysis |
| pH _{zpc} | pH of zero point of charge |
| ROS | Reactive oxygen species |
| SEM | Scanning Electron Microscopy |
| SPCI | Solar photocatalytic inactivation |
| SRFA | Suwannee River Fulvic Acid |
| SRFA _i | Suwannee River Fulvic Acid referring initial conditions |
| SRHA | Suwannee River Humic Acid |
| SRHA _i | Suwannee River Humic Acid referring initial conditions |
| SRNOM | Suwannee River Natural Organic matter |
| SRNOM _i | Suwannee River Natural Organic matter referring initial conditions |
| SS | Saline solution |
| SUVA ₂₅₄ | Specific UV–vis parameter represents UV ₂₅₄ /DOC |
| SUVA ₂₈₀ | Specific UV–vis parameter represents UV ₂₈₀ /DOC |
| WM | Water matrix |
| XPS | X-ray photoelectron spectroscopy |
| XRD | X-ray diffraction |

References

1. Oppenländer, T. *Photochemical Purification of Water and Air: Advanced Oxidation Processes (AOPs): Principles, Reaction Mechanisms, Reactor Concepts*; John Wiley & Sons: Hoboken, NJ, USA, 2007.
2. Silanpää, M.; Matilainen, A.; Lahtinen, T. Characterization of NOM. In *Natural Organic Matter in Water, Characterization and Treatment Methods*; Silanpää, M., Ed.; IWA Publishing: London, UK, 2015.
3. An, T.; Zhao, H.; Wong, P.K. *Advances in Photocatalytic Disinfection*; Springer: Berlin, Germany, 2017.
4. Uyguner-Demirel, C.S.; Birben, N.C.; Bekbolet, M. A comprehensive review on the use of second generation TiO₂ photocatalysts: Microorganism inactivation. *Chemosphere* **2018**, *211*, 420–448. [[CrossRef](#)]
5. Daub, N.A.; Aziz, F.; Aziz, M.; Jaafar, J.; Wan Saleh, W.N.; Yusof, N.; Ismail, A.F. A mini review on parameters affecting the semiconducting oxide photocatalytic microbial disinfection. *Water Air Soil Poll.* **2020**, *231*, 1–13. [[CrossRef](#)]
6. Birben, N.C.; Lale, E.; Pelosato, R.; Cozzarini, L.; Uyguner-Demirel, C.S.; Schmid, C.; Natali Sora, I.; Bekbolet, M. Photocatalytic bactericidal performance of LaFeO₃ under solar light: Kinetics, spectroscopic and mechanistic evaluation. *Water* **2021**, *13*, 1135. [[CrossRef](#)]
7. Turkten, N.; Natali Sora, I.; Tomruk, A.; Bekbolet, M. Photocatalytic degradation of humic acids using LaFeO₃. *Catalysts* **2018**, *8*, 630. [[CrossRef](#)]
8. Caronna, T.; Fontana, F.; Sora, I.N.; Pelosato, R. Chemical synthesis and structural characterization of the substitution compound LaFe_{1-x}Cu_xO₃ (x = 0 – 0.40). *Mater. Chem. Phys.* **2009**, *116*, 645–648. [[CrossRef](#)]
9. Coble, P.G. Characterization of marine and terrestrial NOM in seawater using excitation-emission matrix spectroscopy. *Mar. Chem.* **1996**, *51*, 325–346. [[CrossRef](#)]
10. Baker, A.; Tipping, E.; Thacker, A.; Gondar, D. Relating dissolved organic matter fluorescence and functional properties. *Chemosphere* **2008**, *73*, 1765–1772. [[CrossRef](#)] [[PubMed](#)]
11. Sen-Kavurmaci, S.; Bekbolet, M. Tracing TiO₂ photocatalytic degradation of humic acid in the presence of clay particles by excitation-emission matrix (EEM) fluorescence spectra. *J. Photoch. Photobio. A* **2014**, *82*, 53–61. [[CrossRef](#)]
12. Stedmon, C.A.; Bro, R. Characterizing dissolved organic matter fluorescence with parallel factor analysis: A tutorial. *Limnol. Oceanogr. Meth.* **2008**, *6*, 572–579. [[CrossRef](#)]
13. Darabdharma, G.; Boruah, P.K.; Hussain, N.; Borthakur, P.; Sharma, B.; Sengupta, P.; Das, M.R. Magnetic nanoparticles towards efficient adsorption of Gram positive and Gram negative bacteria: An investigation of adsorption parameters and interaction mechanism. *Colloid Surface A* **2017**, *516*, 161–170. [[CrossRef](#)]
14. Harden, V.P.; Harris, J.O. The isoelectric point of bacterial cells. *J. Bacteriol.* **1953**, *65*, 198–202. [[CrossRef](#)] [[PubMed](#)]
15. IHSS. Available online: <https://humic-substances.org/> (accessed on 3 March 2021).
16. Parrino, F.; García-López, E.; Marcì, G.; Palmisano, L.; Felice, V.; Sora, I.N.; Armelao, L. Cu-substituted lanthanum ferrite perovskites: Preparation, characterization and photocatalytic activity in gas-solid regime under simulated solar light irradiation. *J. Alloy. Comp.* **2016**, *682*, 686–694. [[CrossRef](#)]
17. Chowdhury, I.; Cwiertny, D.M.; Walker, S.L. Combined factors influencing the aggregation and deposition of nano-TiO₂ in the presence of humic acid and bacteria. *Environ. Sci. Technol.* **2012**, *46*, 6968–6976. [[CrossRef](#)] [[PubMed](#)]
18. Elbourne, A.; Chapman, J.; Gelmi, A.; Cozzolino, D.; Crawford, R.J.; Truong, V.K. Bacterial-nanostructure interactions: The role of cell elasticity and adhesion forces. *J. Colloid Interf. Sci.* **2019**, *546*, 192–210. [[CrossRef](#)] [[PubMed](#)]
19. Natali Sora, I.; Fontana, F.; Passalacqua, R.; Ampelli, C.; Perathoner, S.; Centi, G.; Parrino, F.; Palmisano, L. Photoelectrochemical properties of doped lanthanum orthoferrites. *Electrochim. Acta* **2013**, *109*, 710–715. [[CrossRef](#)]
20. Lin, N.; Berton, P.; Moraes, C.; Rogers, R.D.; Tufenkji, N. Nanodarts, nanoblades, and nanopikes: Mechano-bactericidal nanostructures and where to find them. *Adv. Colloid Interfac.* **2018**, *252*, 55–68. [[CrossRef](#)]
21. Cantwell, R.E.; Hofmann, R.; Templeton, M.R. Interactions between humic matter and bacteria when disinfecting water with UV light. *J. Appl. Microbiol.* **2008**, *105*, 25–35. [[CrossRef](#)]
22. Albanese, A.; Walkey, C.D.; Olsen, J.B.; Guo, H.; Emili, A.; Chan, W.C.W. Secreted biomolecules alter the biological identity and cellular interactions of nanoparticles. *ACS Nano* **2014**, *8*, 5515–5526. [[CrossRef](#)]
23. Wang, Q.; Kang, F.; Gao, Y.; Mao, X.; Hu, X. Sequestration of nanoparticles by an EPS matrix reduces the particle specific bactericidal activity. *Sci. Rep.* **2016**, *6*, 1–10. [[CrossRef](#)]
24. Baalousha, M.; Afshinnia, K.; Guo, L. Natural organic matter composition determines the molecular nature of silver nanomaterial-NOM corona. *Environ. Sci. Nano* **2018**, *5*, 868–881. [[CrossRef](#)]
25. Muela, A.; Garcia-Bringas, J.M.; Arana, I.; Barcina, I. Humic materials offer photoprotective effect to *Escherichia coli* exposed to damaging luminous radiation. *Microb. Ecol.* **2000**, *40*, 336–344. [[CrossRef](#)]
26. Ateia, M.; Ran, J.; Fujii, M.; Yoshimura, C. The relationship between molecular composition and fluorescence properties of humic substances. *Int. J. Environ. Sci. Technol.* **2017**, *14*, 867–880. [[CrossRef](#)]
27. Awfa, D.; Ateia, M.; Fujii, M.; Yoshimura, C. Photocatalytic degradation of organic micropollutants: Inhibition mechanisms by different fractions of natural organic matter. *Water Res.* **2020**, *174*, 115643. [[CrossRef](#)]
28. Guerard, J.J.; Miller, P.L.; Trouts, T.D.; Chin, Y.-P. The role of fulvic acid composition in the photosensitized degradation of aquatic contaminants. *Aquat. Sci.* **2009**, *71*, 160–169. [[CrossRef](#)]
29. Uyguner-Demirel, C.S.; Bekbolet, M. Significance of analytical parameters for the understanding of natural organic matter in relation to photocatalytic oxidation. *Chemosphere* **2011**, *84*, 1009–1031. [[CrossRef](#)] [[PubMed](#)]

30. Nelson, D.L.; Cox, M.M. *Lehninger Principles of Biochemistry*, 4th ed.; W.H. Freeman: New York, NY, USA, 2004.
31. Madigan, M.T.; Martinko, J.M. *Brock Biology of Microorganisms*, 11th ed.; Pearson Education, Inc: Upper Saddle River, NJ, USA, 2006.
32. Murphy, K.R.; Hambly, A.; Singh, S.; Henderson, R.K.; Baker, A.; Stuetz, R.; Khan, S.J. Organic matter fluorescence in municipal water recycling schemes: Toward a unified PARAFAC model. *Environ. Sci. Technol.* **2011**, *45*, 2909–2916. [[CrossRef](#)] [[PubMed](#)]
33. Yang, L.; Hur, J.; Zhuang, W. Occurrence and behaviors of fluorescence EEM-PARAFAC components in drinking water and wastewater treatment systems and their applications: A review. *Environ. Sci. Poll. Res.* **2015**, *22*, 6500–6510. [[CrossRef](#)] [[PubMed](#)]
34. Zhao, C.; Wang, Z.; Wang, C.; Li, X.; Wang, C.-C. Photocatalytic degradation of NOM in urban stormwater runoff with TiO₂ nanoparticles under UV light irradiation: EEM-PARAFAC analysis and influence of co-existing inorganic ions. *Environ. Pollut.* **2018**, *243*, 177–188. [[CrossRef](#)]
35. Turong, H.B.; Huy, B.T.; Ly, Q.V.; Lee, Y.-I.; Hur, J. Visible light-activated degradation of natural organic matter (NOM) using zinc-bismuth oxides-graphitic carbon nitride (ZBO-CN) photocatalyst: Mechanistic insights from EEM-PARAFAC. *Chemosphere* **2019**, *224*, 597–606. [[CrossRef](#)]
36. Phong, D.D.; Hur, J. Insight into photocatalytic degradation of dissolved organic matter in UVA/TiO₂ systems revealed by fluorescence EEM-PARAFAC. *Water Res.* **2015**, *87*, 119–126. [[CrossRef](#)]
37. Ly, Q.V.; Kim, H.-C.; Hur, J. Tracking fluorescent dissolved organic matter in hybrid ultrafiltration systems with TiO₂/UV oxidation via EEM-PARAFAC. *J. Membrane Sci.* **2018**, *549*, 275–282. [[CrossRef](#)]
38. Zahra, Z.; Maqbool, T.; Arshad, M.; Badshah, M.A.; Choi, H.-K.; Hur, J. Changes in fluorescent dissolved organic matter and their association with phytoavailable phosphorus in soil amended with TiO₂ nanoparticles. *Chemosphere* **2019**, *227*, 17–25. [[CrossRef](#)] [[PubMed](#)]
39. Phong, D.D.; Hur, J. Using two-dimensional correlation size exclusion chromatography (2D-CoSEC) and EEM-PARAFAC to explore the heterogeneous adsorption behavior of humic substances on nanoparticles with respect to molecular sizes. *Environ. Sci. Technol.* **2018**, *16*, 427–435. [[CrossRef](#)] [[PubMed](#)]
40. Yang, Y.Z.; Peleato, N.M.; Legge, R.L.; Andrews, R.C. Towards real-time detection of wastewater in surface waters using fluorescence spectroscopy. *J. Environ. Sci.* **2019**, *86*, 195–202. [[CrossRef](#)]
41. Tang, J.; Wu, J.; Li, Z.; Cheng, C.; Liu, B.; Chai, Y.; Wang, Y. Novel insights into variation of fluorescent dissolved organic matters during antibiotic wastewater treatment by excitation emission matrix coupled with parallel factor analysis and cosine similarity assessment. *Chemosphere* **2018**, *210*, 843–848. [[CrossRef](#)] [[PubMed](#)]
42. Hedges, J.I. Formation and clay mineral reactions of melanoidins. *Geochim. Cosmochim. Ac.* **1978**, *42*, 69–76. [[CrossRef](#)]
43. Nagata, T. Production mechanisms of dissolved organic matter. In *Microbial Ecology of the Oceans*; Kirchman, D.L., Ed.; Wiley Series in Ecological and Applied Microbiology: Hoboken, NJ, USA, 2000; pp. 121–152.
44. Harvey, G.R.; Boran, D.A.; Chesal, L.A.; Tokar, J.M. The structure of marine fulvic and humic acids. *Mar. Chem.* **1983**, *12*, 119–132. [[CrossRef](#)]
45. Harvey, G.R.; Boran, D.A.; Piotrowicz, S.R.; Weisel, C.P. Synthesis of marine humic substances from unsaturated lipids. *Nature* **1984**, *309*, 244–246. [[CrossRef](#)]
46. Sharon, M.; Datta, S.; Shah, S.; war Sharon, M.; Soga, T.; Afre, R. Photocatalytic degradation of *E. coli* and *S. aureus* by multi walled carbon nanotubes. *Carbon Lett.* **2007**, *8*, 184–190. [[CrossRef](#)]
47. Carré, G.; Hamon, E.; Ennahar, S.; Estner, M.; Lett, M.-C.; Horvatovich, P.; Gies, J.-P.; Keller, V.; Keller, N.; Andrea, P. TiO₂ photocatalysis damages lipids and proteins in *Escherichia coli*. *Appl. Environ. Microb.* **2014**, *80*, 2573–2581. [[CrossRef](#)]
48. Kiwi, J.; Nadtochenko, V. Evidence for the mechanism of photocatalytic degradation of the bacterial wall membrane at the TiO₂ interface by ATR-FTIR and Laser Kinetic Spectroscopy. *Langmuir* **2005**, *21*, 4631–4641. [[CrossRef](#)] [[PubMed](#)]
49. Nadtochenko, V.A.; Rincon, A.G.; Stanca, S.E.; Kiwi, J. Dynamics of *E. coli* membrane cell peroxidation during TiO₂ photocatalysis studied by ATR-FTIR spectroscopy and AFM microscopy. *J. Photoch. Photobio. A* **2005**, *169*, 131–137. [[CrossRef](#)]
50. Rtimi, S.; Sanjines, R.; Andrzejczuk, M.; Pulgarin, C.; Kulik, A.; Kiwi, J. Innovative transparent non-scattering TiO₂ bactericidal thin films inducing increased *E. coli* cell wall fluidity. *Surf. Coat. Tech.* **2014**, *254*, 333–343. [[CrossRef](#)]
51. Abazari, R.; Sanati, S.; Saghatforoush, L.A. A unique and facile preparation of lanthanum ferrite nanoparticles in emulsion nanoreactors: Morphology, structure, and efficient photocatalysis. *Mat. Sci. Semicon. Proc.* **2014**, *25*, 301–306. [[CrossRef](#)]
52. Foster, H.A.; Ditta, I.B.; Varghese, S.; Steele, A. Photocatalytic disinfection using titanium dioxide: Spectrum and mechanism of antimicrobial activity. *Appl. Microbiol. Biot.* **2011**, *90*, 1847–1868. [[CrossRef](#)] [[PubMed](#)]
53. FTIR, 13C-NMR and Fluorescence Spectra of IHSS Standards. Available online: <https://humic-substances.org/ftir-13c-nmr-and-fluorescence-spectra/> (accessed on 3 March 2021).